

Magnetic Braking in Differentially Rotating, Relativistic Stars

Yuk Tung Liu and Stuart L. Shapiro*

Department of Physics, University of Illinois at Urbana-Champaign, Urbana, IL 61801

We study the magnetic braking and viscous damping of differential rotation in incompressible, uniform density stars in general relativity. Differentially rotating stars can support significantly more mass in equilibrium than nonrotating or uniformly rotating stars, according to general relativity. The remnant of a binary neutron star merger or supernova core collapse may produce such a “hypermassive” neutron star. Although a hypermassive neutron star may be stable on a dynamical timescale, magnetic braking and viscous damping of differential rotation will ultimately alter the equilibrium structure, possibly leading to delayed catastrophic collapse. Here we treat the slow-rotation, weak-magnetic field limit in which $E_{\text{rot}} \ll E_{\text{mag}} \ll W$, where E_{rot} is the rotational kinetic energy, E_{mag} is the magnetic energy, and W is the gravitational binding energy of the star. We assume the system to be axisymmetric and solve the MHD equations in both Newtonian gravitation and general relativity. For an initially uniform magnetic field parallel to the rotation axis in which we neglect viscosity, the Newtonian case can be solved analytically, but the other cases we consider require a numerical integration. Toroidal magnetic fields are generated whenever the angular velocity varies along the initial poloidal field lines. We find that the toroidal fields and angular velocities oscillate independently along each poloidal field line, which enables us to transform the original 2+1 equations into 1+1 form and solve them along each field line independently. The incoherent oscillations on different field lines stir up turbulent-like motion in tens of Alfvén timescales (“phase mixing”). In the presence of viscosity, the stars eventually are driven to uniform rotation, with the energy contained in the initial differential rotation going into heat. Our evolution calculations serve as qualitative guides and benchmarks for future, more realistic MHD simulations in full 3+1 general relativity.

PACS numbers: 04.40.Dg, 95.30.Qd, 97.60.Jd

I. INTRODUCTION

New-born neutron stars formed from core collapse supernovae, accretion induced collapse of white dwarfs, and coalescence of neutron star binaries are likely to be differentially rotating [1–6]. Differential rotation will cause a frozen-in poloidal magnetic field to wind up and generate a strong toroidal field. The back-reaction of the magnetic stresses on the fluid motion – magnetic braking – will destroy the initial differential rotation and can result in a significant change in the structure and dynamics of the star.

Differentially rotating neutron stars can support significantly more rest mass than their nonrotating or uniformly rotating counterparts, creating “hypermassive” neutron stars [16, 17]. Such hypermassive neutron stars can form from the coalescence of neutron star binaries [5, 6]. The stabilization arising from differential rotation, although expected to last for many dynamical timescales, will ultimately be destroyed by magnetic braking and/or viscosity [16, 38]. These processes drive the star to uniform rotation, which cannot support the excess mass, and can lead to “delayed” catastrophic collapse, possibly accompanied by some mass loss.

Conservation of angular momentum implies that the nascent neutron stars formed from core collapse super-

novae or accretion induced collapse of white dwarfs are rapidly and differentially rotating. These neutron stars may develop a nonaxisymmetric bar-mode instability that might be detectable as a quasi-periodic gravitational wave by gravitational wave detectors, such as LIGO, VIRGO, GEO and TAMA. The *dynamical* bar-instability usually develops when the ratio $\beta = T/W$ is high enough, e.g. $\beta \gtrsim 0.25 - 0.27$ [4, 18], where T is the rotational kinetic energy and W is the gravitational binding energy (however, for extreme degrees of differential rotation a bar-instability may also develop for stars with very low β [19–21]; moreover, an $m = 1$ one-armed spiral mode may also become dynamically unstable for stars with a very soft equation of state and a high degree of differential rotation [31, 32]). A hot, proto-neutron star formed a few milliseconds after core bounce may not have a sufficiently high value of β to trigger the dynamical bar-instability immediately. However, the instability might develop after about 20 seconds, after which neutrinos will have carried away most of the thermal energy, causing the star to contract further and β to exceed the threshold value for the bar-instability. If the proto-neutron star has a strong magnetic field ($B \gtrsim 10^{12}G$), magnetic braking could significantly change the angular momentum distribution during the neutrino cooling phase and might suppress the bar-instability [4]. On the other hand, the *secular* bar-instability could develop at much lower β [7] on a longer timescale. Once again, a small, frozen-in seed magnetic field could be wound up to sufficiently high strength by differential rotation to suppress the secular instability over this timescale.

*Department of Astronomy & NCSA, University of Illinois at Urbana-Champaign, Urbana, IL 61801

Short-duration gamma-ray bursts (GRBs) are thought to result from binary neutron star mergers [22], or tidal disruptions of neutron stars by black holes [2]. Long-duration GRBs likely result from the collapse of rotating, massive stars which form black holes, followed by supernova explosions [15, 23]. In current scenarios, the burst is powered by the extraction of rotational energy from the neutron star or black hole, or from the remnant disk material formed around the black hole [24]. Strong magnetic fields provide the likely mechanism for extracting this energy on the required timescale and driving collimated GRB outflows in the form of relativistic jets [25–27]. Even if the initial magnetic fields are weak, they can be amplified to the required values by differential motions or dynamo action.

The r -mode instability has recently been proposed as a possible mechanism for limiting the angular velocities in neutron stars and producing observable quasi-periodic gravitational waves [39–42]. However, preliminary calculations (see Refs. [43–45] and references therein) suggest that if the stellar magnetic field is strong enough, r -mode oscillations will not occur. Even if the initial field is weak, fluid motions produced by these oscillations may amplify the magnetic field and eventually distort or suppress the r -modes altogether (r -mode oscillations may also be suppressed by nonlinear mode coupling [46–48] or hyperon bulk viscosity [49–51]).

In a different context, supermassive stars (SMSs) may form in the early universe, and their catastrophic collapse may provide the seeds of supermassive black holes (SMBHs) observed in galaxies and quasars (see Refs. [28–30] for discussion and references). If an SMS maintains uniform rotation as it cools and contracts, it will ultimately arrive at the onset of a relativistic radial instability, triggering coherent dynamical collapse to an SMBH and giving rise to a burst of gravitational waves [33, 34]. If an SMS is differentially rotating, cooling and contraction will instead lead to the unstable formation of bars or spiral arms prior to collapse and the production of quasi-periodic gravitational waves [35, 36]. Since magnetic fields and turbulent viscosity provide the principal mechanisms that can damp differential rotation in such stars [37, 38], their role is therefore crucial in determining the fate of these objects.

Motivated by the importance of magnetic fields in differentially rotating relativistic stars, Shapiro performed a simple, Newtonian, MHD calculation showing some of the effects of magnetic braking ([38], hereafter Paper I). In his simplified model, the star is idealized as a differentially rotating, infinite cylinder consisting of a homogeneous, incompressible conducting gas. The magnetic field is taken to be purely radial initially and is allowed to evolve according to the ideal MHD equations (flux-freezing). The calculation shows that differential rotation generates a toroidal magnetic field, which reacts back on the fluid flow. In the absence of viscous dissipation, the toroidal field energy and rotational kinetic energy in differential motion undergo periodic oscillations on the

Alfvén timescale. The magnitude of the oscillations is independent of the initial magnetic field strength; only the growth and oscillation timescale depends on the magnitude of the seed field. If viscosity is present, or if some of the Alfvén waves are allowed to propagate out of the star and into an ambient plasma atmosphere, the oscillations are damped, rotational energy is dissipated, and the star is driven to uniform rotation.

Recently, Cook, Shapiro, and Stephens ([52], hereafter Paper II) generalized Shapiro’s calculations for compressible stars. In their model, the star is idealized as a differentially rotating, infinite cylinder supported by a polytropic equation of state. They performed Newtonian MHD simulations for differentially rotating stars with various polytropic indices and different values of β . They found that when β is below the upper (mass-shedding) limit for uniform rotation, β_{max} , magnetic braking results in oscillations of the induced toroidal fields and angular velocities, and the star pulsates stably. However, when β exceeds β_{max} , their calculations suggest that the core contracts significantly, but quasistatically, while the outer layers are ejected to large radii to form a wind or an ambient disk.

In this paper, we consider another idealized, but useful, model to explore the effects of general relativity on magnetic braking and viscous damping of differential rotation in stars. Our star is idealized as an incompressible, slowly differentially rotating sphere of uniform density, threaded by a seed poloidal magnetic field at time $t = 0$. To simplify the calculations, we restrict our analysis to the case in which $E_{\text{rot}} \ll E_{\text{mag}} \ll W$, where $E_{\text{rot}} = T$ is the rotational kinetic energy, and E_{mag} is the magnetic energy. The condition $E_{\text{mag}} \gg E_{\text{rot}}$ is equivalent to the condition that the Alfvén timescale t_A is much shorter than the rotation period P_{rot} . The condition that $E_{\text{mag}} \ll W$ guarantees that the magnetic field is small in comparison to the internal pressure forces and gravitational field. We perform MHD evolution calculations in Newtonian gravity, first as a “warm-up”, and then in full general relativity, for various initial field configurations. For an initial magnetic field parallel to the rotation axis in which we neglect viscosity, the Newtonian equations can be solved analytically, but the other cases we consider require numerical integration. Adopting axisymmetry, our MHD equations are two-dimensional, as opposed to one-dimensional in Papers I and II. We found that this extra degree of freedom changes the description of magnetic braking. We found that the angular velocity and toroidal magnetic field undergo periodic oscillations along the initial poloidal field lines, in the absence of viscosity. However, the oscillation frequencies are different along each poloidal field line. The incoherent oscillations on different field lines eventually destroys the laminar flow and creates irregular velocity fields across the poloidal field lines. This effect has been studied in Newtonian MHD and is sometimes referred to as “phase mixing” (see [67] and references therein). We demonstrate that this phase mixing effect is also present in relativistic

MHD.

In the situation where the Alfvén timescale is much shorter than the rotation period, which is the limit we consider in this paper, the phase mixing may create turbulent-like flows in tens of Alfvén timescales. We also studied the effect of magnetic braking in the presence of viscosity. We found that, not surprisingly, the star eventually will be driven to uniform rotation by the combined action of the magnetic fields and viscosity.

Although our analysis in this paper is restricted to the early phases of evolution in the slow-rotation, weak-magnetic field limit, we are able to solve the full nonlinear MHD equations for a highly relativistic, differentially rotating star. Our calculations serve as qualitative guides and benchmarks for future, more realistic MHD simulations in full 3+1 general relativity.

We structure this paper as follows: in Section II, we describe our model in detail. We derive and analyze the Newtonian MHD equations in Section III. In Section IV, we derive the analogous relativistic MHD equations using the 3+1 formalism presented by Baumgarte and Shapiro [54]. We then rewrite the MHD equations in nondimensional form in Section V, and present our numerical results in Section VI. Finally, we summarize and discuss our results in Section VII.

II. MODEL

We consider an incompressible, rotating equilibrium star of uniform density (i.e. a polytrope of index $n = 0$). At time $t = 0$, the star is assumed to rotate slowly and differentially with a small axisymmetric poloidal magnetic field. We assume that both the rotational kinetic energy and the magnetic energy are small compared to the gravitational binding energy. In Newtonian gravity, the deviation from the spherical solution is of second order in the magnetic field strength and/or in the magnitude of angular velocity and is therefore neglected in our treatment. In general relativity, the leading order correction to the metric comes from the dragging of inertial frames, which is of first order. We therefore neglect the deformation of the star in Newtonian gravity, but keep the frame dragging term in general relativity.

As discussed in Papers I and II, differential rotation twists up the frozen-in poloidal magnetic field and generates a toroidal field in the star. The toroidal field causes a shear stress on the fluid and this stress changes the angular velocity profile on the Alfvén timescale of the poloidal field. Unlike the cases studied in Papers I and II, the changes in angular velocity will generate typically a meridional current. The interaction of magnetic field and the meridional current may develop MHD instabilities and result in turbulence [53].

In this paper, we consider the case in which the Alfvén timescale is much shorter than the rotation period. In particular, we consider the case in which $W \gg E_{\text{mag}} \gg E_{\text{rot}}$. The condition $E_{\text{mag}} \gg E_{\text{rot}}$ is equivalent to the

condition that $v_A \gg \Omega R$, where v_A is a typical Alfvén speed, Ω is a typical angular velocity inside the star, and R is the radius of the star. It can be shown (see Appendix A) that the meridional current can be ignored in the early phase of the magnetic braking. In this paper, we focus on the effect of magnetic braking before the meridional current builds up. We assume the system remains axisymmetric on the timescale of interest.

III. NEWTONIAN EQUATIONS

A. Basic Equations

We start with the MHD equations for a perfectly conducting, incompressible, viscous Newtonian fluid (see, e.g. [55, 61])

$$\frac{\partial \mathbf{B}}{\partial t} = \nabla \times (\mathbf{v} \times \mathbf{B}), \quad (1)$$

$$\rho \left(\frac{\partial \mathbf{v}}{\partial t} + \mathbf{v} \cdot \nabla \mathbf{v} \right) = -\nabla p - \rho \nabla \Phi - \nabla \left(\frac{B^2}{8\pi} \right) + \frac{1}{4\pi} (\mathbf{B} \cdot \nabla) \mathbf{B} \\ + \nabla \cdot (\eta \boldsymbol{\sigma}) + \nabla (\zeta \nabla \cdot \mathbf{v}), \quad (2)$$

$$\nabla \cdot \mathbf{v} = 0, \quad (3)$$

$$\nabla^2 \Phi = 4\pi G \rho, \quad (4)$$

where η and ζ are the coefficients of shear and bulk viscosity, respectively, and in general are functions of pressure and temperature. The components of the shear tensor in Cartesian coordinates are given by

$$\sigma_{ij} = \partial_i v_j + \partial_j v_i - \frac{2}{3} \delta_{ij} \nabla \cdot \mathbf{v}. \quad (5)$$

For an incompressible fluid, Eq. (3) allows us to write

$$\frac{\partial \mathbf{B}}{\partial t} = \mathbf{B} \cdot \nabla \mathbf{v} - \mathbf{v} \cdot \nabla \mathbf{B}, \quad (6)$$

$$\frac{\partial \mathbf{v}}{\partial t} + \mathbf{v} \cdot \nabla \mathbf{v} = -\frac{1}{\rho} \nabla p - \nabla \Phi - \nabla \left(\frac{B^2}{8\pi} \right) + \frac{1}{4\pi \rho} \mathbf{B} \cdot \nabla \mathbf{B} \\ + \nabla \cdot (\nu \boldsymbol{\sigma}), \quad (7)$$

where $\nu = \eta/\rho$.

In order to make a direct comparison between Newtonian and relativistic MHD equations, we adopt some conventions used in relativity. For the spherical coordinate system (r, θ, ϕ) , we introduce three orthonormal unit basis vectors

$$\mathbf{e}_{\hat{r}} = \sin \theta \cos \phi \mathbf{e}_x + \sin \theta \sin \phi \mathbf{e}_y + \cos \theta \mathbf{e}_z \quad (8)$$

$$\mathbf{e}_{\hat{\theta}} = \cos \theta \cos \phi \mathbf{e}_x + \cos \theta \sin \phi \mathbf{e}_y - \sin \theta \mathbf{e}_z \quad (9)$$

$$\mathbf{e}_{\hat{\phi}} = -\sin \phi \mathbf{e}_x + \cos \phi \mathbf{e}_y, \quad (10)$$

where \mathbf{e}_x , \mathbf{e}_y and \mathbf{e}_z are the usual Cartesian unit basis vectors. The basis vectors satisfy $\mathbf{e}_{\hat{i}} \cdot \mathbf{e}_{\hat{j}} = \delta_{ij}$, where i and j denote r , θ and ϕ . Any vector \mathbf{V} can be expanded in these three basis vectors as

$$\mathbf{V} = V^{\hat{r}} \mathbf{e}_{\hat{r}} + V^{\hat{\theta}} \mathbf{e}_{\hat{\theta}} + V^{\hat{\phi}} \mathbf{e}_{\hat{\phi}}. \quad (11)$$

We also define the coordinate basis vectors

$$\mathbf{e}_r = \mathbf{e}_{\hat{r}} , \quad \mathbf{e}_\theta = r\mathbf{e}_{\hat{\theta}} , \quad \mathbf{e}_\phi = r \sin \theta \mathbf{e}_{\hat{\phi}} , \quad (12)$$

which satisfy $\mathbf{e}_i \cdot \mathbf{e}_j = g_{ij}$. Here the spatial metric tensor satisfies

$$g_{rr} = 1 , \quad g_{\theta\theta} = r^2 , \quad g_{\phi\phi} = r^2 \sin^2 \theta , \quad (13)$$

and all the off-diagonal components of g_{ij} are zeros. Any vector \mathbf{V} can be expanded in these coordinate basis vectors as

$$\mathbf{V} = V^r \mathbf{e}_r + V^\theta \mathbf{e}_\theta + V^\phi \mathbf{e}_\phi , \quad (14)$$

hence we have

$$V^r = V^{\hat{r}} , \quad V^\theta = V^{\hat{\theta}}/r , \quad V^\phi = V^{\hat{\phi}}/r \sin \theta . \quad (15)$$

We assume the system is axisymmetric and ignore the meridional components of velocity (see Appendix A). We therefore set $v^r = v^\theta = 0$, and assume there is no toroidal field at time $t = 0$, $B^\phi(0; r, \theta) = 0$. We also assume that the star has a small amount of rotation $v^\phi = \Omega(0; r, \theta)$ and an initial poloidal field $\mathbf{B}(0; r, \theta) = B^r(0; r, \theta)\mathbf{e}_r + B^\theta(0; r, \theta)\mathbf{e}_\theta$. Equation (6) immediately gives $\partial_t B^r = \partial_t B^\theta = 0$. Hence the poloidal field, which we shall designate $\mathbf{B}(0)$, does not evolve with time. Equations (6) and (7) simplify to yield

$$\partial_t B^\phi = B^j(0)\partial_j \Omega , \quad (16)$$

$$\partial_t \Omega = \frac{1}{4\pi\rho r^2 \sin^2 \theta} B^j(0)\partial_j(r^2 \sin^2 \theta B^\phi) + (\partial_t \Omega)_{\text{vis}} , \quad (17)$$

where j denotes r and θ , and the usual summation convention is adopted. In spherical coordinates, this viscous term takes the form

$$(\partial_t \Omega)_{\text{vis}} = \frac{1}{r^4} \partial_r(\nu r^4 \partial_r \Omega) + \frac{1}{r^2 \sin^3 \theta} \partial_\theta(\nu \sin^3 \theta \partial_\theta \Omega) . \quad (18)$$

The toroidal field is generated via Alfvén waves, which cannot propagate in vacuum. Hence the toroidal field cannot be carried outside the star. This fact, together with Eq. (16), leads to the boundary condition

$$B^\phi(t, R, \theta) = 0 = B^j(0)\partial_j \Omega|_{r=R} , \quad (19)$$

where R is the radius of the star.

B. Initial Magnetic Field

In order to solve the MHD equations (16) and (17), we need to specify the poloidal field $\mathbf{B}(0)$ inside the star. In this paper, we consider simple models of the internal magnetic field. A systematic way to generate an axisymmetric poloidal magnetic field is to assume that $\nabla \times \mathbf{B}(0) = 0$ inside the star. This corresponds to assuming that no internal electromagnetic currents are

present in the stellar interior. Such a curl-free magnetic field can be generated only by a toroidal current on the surface of the star. It follows that we can write $\mathbf{B}(0) = \nabla \Phi_m$, where Φ_m is a scalar function. The constraint $\nabla \cdot \mathbf{B}(0) = 0$ implies $\nabla^2 \Phi_m = 0$. The general axisymmetric solutions to this equation that are regular at the origin can be expanded in terms of Legendre polynomials according to

$$\Phi_m(r, \theta) = \sum_{l=0}^{\infty} a_l r^l P_l(\cos \theta) , \quad (20)$$

where a_l are constants.

The $l = 0$ mode corresponds to the trivial solution $\mathbf{B}(0) = 0$. For $l = 1$, we have $\Phi_m = B_0 r \cos \theta$, where B_0 is a constant. Hence $B^r(0) = B_0 \cos \theta$ and $B^\theta(0) = -B_0 \sin \theta$, or $\mathbf{B}(0) = B_0 \mathbf{e}_z$, which is a uniform field along the rotation axis of the star. It follows from Eqs. (16) and (17) that if the angular velocity is constant on cylinders, i.e. $\partial_z \Omega = 0$, there will be no magnetic braking in the absence of viscosity. However, it can be proven (see, e.g. Ref. [58], Section 4.3) that a barotropic star in rotational equilibrium must have such a rotation profile. Numerical simulations of core collapse supernovae also suggest that the resulting neutron stars have angular velocity approximately constant on cylinders (see e.g., [59]). Hence we also consider the $l = 2$ field in which $\Phi_m = B_0 r^2 (3 \cos^2 \theta - 1)/R$, where R is the radius of the star. The associated magnetic field is

$$B^r = B_0 \left(\frac{r}{R} \right) (3 \cos^2 \theta - 1) \quad (21)$$

$$B^\theta = -3B_0 \left(\frac{r}{R} \right) \sin \theta \cos \theta . \quad (22)$$

Figure 1 shows the field lines for this $l = 2$ field. Magnetic braking will occur in this case even when $\partial_z \Omega = 0$. As will be seen later, the MHD equations for the $l = 1$ field is much simpler than the equations for the $l = 2$ field. For pedagogical purpose, we find it useful to study the magnetic braking for the $l = 1$ field first, where we adopt an *ad hoc* rotation law with $\partial_z \Omega \neq 0$. We then study magnetic braking for the $l = 2$ field with a more realistic rotation law.

It is easy to prove that any axisymmetric poloidal field can be generated by a vector potential of the form

$$\mathbf{A}(\mathbf{x}) = A^{\hat{\phi}}(r, \theta) \mathbf{e}_{\hat{\phi}} . \quad (23)$$

For the $l = 1$ field, we have

$$A^{\hat{\phi}}(r, \theta) = \frac{1}{2} B_0 r \sin \theta . \quad (24)$$

For the $l = 2$ field, we have

$$A^{\hat{\phi}}(r, \theta) = B_0 \left(\frac{r^2}{R} \right) \sin \theta \cos \theta . \quad (25)$$

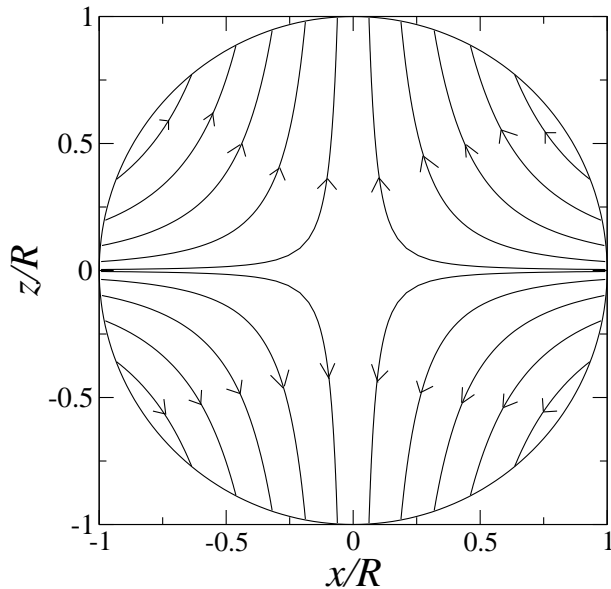


FIG. 1: Field lines of the $l = 2$ poloidal magnetic field on the $y = 0$ (meridional) plane.

The vector potential will be useful in Section III D. It is also a convenient way to generate axisymmetric poloidal fields in relativistic case (see Section IV C).

C. Conserved Integrals

The MHD equations (16) and (17) admit two non-trivial integrals of motion, one expressing the conservation of energy and the other conservation of angular momentum.

Multiplying Eq. (17) by $\rho r^2 \sin^2 \theta$, integrating over the volume of the star and using the boundary condition $B^\phi(r = R) = 0$ and the Maxwell equation $\nabla \cdot \mathbf{B}(0) = 0$, we find that the angular momentum

$$J = \int \rho \Omega r^2 \sin^2 \theta dV \quad (26)$$

is conserved.

To derive the energy integral, we first multiply Eq. (16) by $r^2 \sin^2 \theta B^\phi / 4\pi$ and integrate over the volume of the star. We obtain, after integration by parts,

$$\frac{d}{dt} \int \frac{(B^\phi)^2}{8\pi} dV = -\frac{1}{4\pi} \int \Omega B^j(0) \partial_j (r^2 \sin^2 \theta B^\phi) dV, \quad (27)$$

where we have used $B^\phi = r \sin \theta B^\phi$, the boundary condition $B^\phi(r = R) = 0$ and $\nabla \cdot \mathbf{B}(0) = 0$. Multiplying Eq. (16) by $\rho \Omega r^2 \sin^2 \theta$ and integrating over the volume of the star, we obtain

$$\frac{d}{dt} \int \frac{1}{2} \rho \Omega^2 r^2 \sin^2 \theta dV = \frac{1}{4\pi} \int B^j(0) \partial_j (r^2 \sin^2 \theta B^\phi) dV$$

$$+ \int \rho r^2 \sin^2 \theta (\partial_t \Omega)_{\text{vis}} dV. \quad (28)$$

Hence we have

$$\frac{d}{dt} (E_{\text{rot}} + E_{\text{mag}}) = \int \rho \Omega r^2 \sin^2 \theta (\partial_t \Omega)_{\text{vis}} dV, \quad (29)$$

where

$$E_{\text{rot}} = \int \frac{1}{2} \rho \Omega^2 r^2 \sin^2 \theta dV, \quad (30)$$

$$E_{\text{mag}} = \int \frac{(B^\phi)^2}{8\pi} dV. \quad (31)$$

Note that we only include the magnetic energy associated with the toroidal field in E_{mag} . One could also include the energy associated with the poloidal field and still has the energy conservation since the poloidal field does not change with time. If we define

$$E_{\text{vis}}(t) = \int_0^t \dot{E}_{\text{vis}}(t') dt', \quad (32)$$

where

$$\dot{E}_{\text{vis}} = \int \rho \Omega r^2 \sin^2 \theta (\partial_t \Omega)_{\text{vis}} dV, \quad (33)$$

we have

$$\frac{d}{dt} (E_{\text{rot}} + E_{\text{mag}} + E_{\text{vis}}) = 0. \quad (34)$$

Hence the total energy $E = E_{\text{rot}} + E_{\text{mag}} + E_{\text{vis}}$ is conserved.

To compute \dot{E}_{vis} , we use Eq. (18) for $(\partial_t \Omega)_{\text{vis}}$. After integration by parts, we obtain

$$\dot{E}_{\text{vis}} = \int \eta r^2 \sin^2 \theta \left[(\partial_r \Omega)^2 + \frac{(\partial_\theta \Omega)^2}{r^2} \right] dV, \quad (35)$$

$$= \int \eta r^2 \sin^2 \theta (\nabla \Omega)^2 dV. \quad (36)$$

We note that, consistent with the nonrelativistic MHD approximation, the electric field energy $E^2/8\pi$ is not included in Eq. (34) and the angular momentum of the electromagnetic field is not included in Eq. (26) [56].

The motivation for monitoring the conservation equations during the evolution is twofold: physically, evaluating the individual terms enables us to track how the initial rotational energy and angular momentum in the fluid are transformed and/or dissipated; computationally, monitoring how well the conservation equations are satisfied provides a check on the numerical integration scheme.

D. Build up of Small-Scale Structure: Phase Mixing

In the absence of viscosity, the MHD equations (16) and (17) become

$$\partial_t B^\phi = B^j(0) \partial_j \Omega, \quad (37)$$

$$\partial_t \Omega = \frac{1}{4\pi\rho r^2 \sin^2 \theta} B^j(0) \partial_j (r^2 \sin^2 \theta B^\phi). \quad (38)$$

These equations have a peculiar property that will induce the growth of small-scale fluctuations in the fluid's angular motion and toroidal field. To study this, we first notice that the 2+1 MHD equations can be reduced to a 1+1 problem if we can find a coordinate transformation $u = u(r, \theta)$, $v = v(r, \theta)$ such that

$$B^j(0) \frac{\partial}{\partial x^j} = \kappa(u, v) \frac{\partial}{\partial u}. \quad (39)$$

If such coordinates exist, the MHD equations (37) and (38) reduce to the following 1+1 form:

$$\partial_t B^\phi = \kappa(u, v) \partial_u \Omega, \quad (40)$$

$$\partial_t \Omega = \frac{1}{4\pi\rho r^2 \sin^2 \theta} \kappa(u, v) \partial_u (r^2 \sin^2 \theta B^\phi). \quad (41)$$

Here r and θ are treated as implicit functions of u and v . Applying Eq. (39) to u and v , we obtain the conditions that must be satisfied by u and v :

$$B^j(0) \frac{\partial u}{\partial x^j} = \kappa, \quad (42)$$

$$B^j(0) \frac{\partial v}{\partial x^j} = 0. \quad (43)$$

Such coordinates indeed exist and are easy to find. Equation (43) requires that v is constant along a given poloidal field line. Since the field lines do not cross and cover the volume insider the star, v is a valid coordinate, labeling each field line. One way to find v is by way of the vector potential. The covariant ϕ -component of the vector potential is defined as

$$A_\phi = r \sin \theta A^{\hat{\phi}}. \quad (44)$$

It follows from $\mathbf{B}(0) = \nabla \times (A^{\hat{\phi}} \mathbf{e}_\phi)$ that

$$B^r(0) = \frac{\partial_\theta A_\phi}{r^2 \sin^2 \theta}, \quad (45)$$

$$B^\theta(0) = -\frac{\partial_r A_\phi}{r^2 \sin^2 \theta}. \quad (46)$$

It follows that $B^j(0) \partial_j A_\phi = 0$. Hence we can choose $v = f(A_\phi)$, where f is any function with a continuous first derivative. The coordinate u is arbitrary as long as it is independent of v . The function κ is then determined by Eq. (42).

It is obvious that for the $l = 1$ field ($\mathbf{B}(0) = B_0 \mathbf{e}_z$), the preferred coordinates are cylindrical coordinates ($u = z = r \cos \theta$ and $v = \varpi = r \sin \theta$), for which $\kappa = B_0$. The MHD equations become

$$\partial_t B^\phi = B_0 \partial_z \Omega, \quad (47)$$

$$\partial_t \Omega = \frac{B_0}{4\pi\rho} \partial_z B^\phi, \quad (48)$$

which can be solved analytically (see the next subsection).

The situation for the $l = 2$ field is more complicated. The covariant ϕ -component of the vector potential that generates the field is $A_\phi = B_0 (r^3/R) \sin^2 \theta \cos \theta$ [see Eq. (25)]. We choose

$$u = -r^2 (3 \cos^2 \theta - 1), \quad (49)$$

$$v = r^3 \sin^2 \theta \cos \theta. \quad (50)$$

The variable u is chosen so that $\nabla u \propto \mathbf{B}(0)$, hence $u \propto \Phi_m$, and $\nabla u \cdot \nabla v = 0$. Equation (42) gives

$$\kappa = -\frac{2B_0 r^2}{R} (3 \cos^2 \theta + 1). \quad (51)$$

The MHD equations become

$$\partial_t B^\phi = -\frac{2B_0 r^2}{R} (3 \cos^2 \theta + 1) \partial_u \Omega \quad (52)$$

$$\partial_t \Omega = -\frac{2B_0}{4\pi\rho R} [r^2 (3 \cos^2 \theta + 1) \partial_u B^\phi + B^\phi]. \quad (53)$$

Here r and θ are regarded as implicit functions of u and v .

The set of equations (40) and (41) is effectively a 1+1 system, with v serving as an effective ‘‘mode’’ number. There is no coupling between different values of v . The toroidal field B^ϕ and angular velocity Ω oscillate independently along each poloidal field line. The oscillation frequencies are determined by the boundary condition $B^\phi(r = R) = 0$ and are in general different on different field lines. As a result, the toroidal field and angular velocity on different poloidal field lines will lose coherence. Small-scale structure will gradually build up. This is commonly referred to *phase mixing* [67, 68]. In the next subsection, we demonstrate this phenomenon quantitatively via an analytic solution.

E. Analytic Solution for the $l = 1$ field

Combining Eqs. (47) and (48), we obtain

$$\partial_t^2 B^\phi = v_A^2 \partial_z^2 B^\phi, \quad (54)$$

where $v_A = B_0/\sqrt{4\pi\rho}$ is the Alfvén velocity associated with the poloidal field. This is a simple wave equation; a similar equation arises for Ω . We are interested in the solution in which Ω is symmetric under $z \rightarrow -z$ and $B^\phi = 0$ at $t = 0$. The general solution that satisfies the boundary condition $B^\phi(r = R) = 0$ is

$$B^\phi(t; \varpi, z) = B_0 \left(\frac{\varpi}{R} \right) \sum_{n=1}^{\infty} C_n(\varpi) \sin[k_n(\varpi)z] \times \sin[\omega_n(\varpi)t], \quad (55)$$

$$\Omega(t; \varpi, z) = \Omega(0; \varpi, z) + \frac{v_A}{R} \sum_{n=1}^{\infty} C_n(\varpi) \cos[k_n(\varpi)z] \times \{1 - \cos[\omega_n(\varpi)t]\}, \quad (56)$$

where

$$k_n(\varpi) = \frac{n\pi}{\sqrt{R^2 - \varpi^2}}, \quad \omega_n(\varpi) = v_A k_n(\varpi). \quad (57)$$

The functions $C_n(\varpi)$ are determined by the initial differential angular velocity distribution $\Omega(0; \varpi, z)$:

$$C_n(\varpi) = \frac{2R}{\omega_n \sqrt{R^2 - \varpi^2}} \int_0^{\sqrt{R^2 - \varpi^2}} [\partial_z \Omega(0; \varpi, z)] \sin k_n z dz. \quad (58)$$

We see clearly from Eq. (57) that the characteristic frequency on each field line is different. Incoherence and small-scale structure will build up after a certain time. To be precise, for a given ϖ and a small length scale ΔL , the eigenfrequency $\omega_n(\varpi)$ changes on this length scale by an amount

$$\Delta\omega_n = \frac{n\pi v_A \varpi}{(R^2 - \varpi^2)^{3/2}} \Delta L. \quad (59)$$

The field $B^{\hat{\phi}}$ and angular velocity Ω will lose coherence over ΔL on a timescale

$$t_{\text{coh}} \approx \frac{2\pi}{\Delta\omega_n} = \frac{2R^2}{n\varpi\Delta L} \left(1 - \frac{\varpi^2}{R^2}\right)^{3/2} t_A, \quad (60)$$

where the Alfvén time $t_A = R/v_A$. For $\varpi = R/2$, $\Delta L = R/10$ and $n = 1$, we have $t_{\text{coh}} \approx 26t_A$. The phase mixing will eventually lead to chaotic-like motion over any finite radial scale.

The solution for the $l = 2$ case must be obtained numerically. We postpone a discussion of this case, and the effects of viscous damping, for the fully relativistic treatment.

IV. GENERAL RELATIVISTIC MHD

A. 3+1 Decomposition

In this subsection, we briefly summarize the general relativistic MHD formulation presented in Ref. [54]. Hereafter, we adopt geometrized units and set $c = G = 1$.

We start with the standard 3+1 decomposition of the metric:

$$ds^2 = -\alpha^2 dt^2 + \gamma_{ij}(dx^i + \beta^i dt)(dx^j + \beta^j dt). \quad (61)$$

The spatial metric γ_{ab} is related to the full metric g_{ab} by

$$\gamma_{ab} = g_{ab} + n_a n_b, \quad (62)$$

where n^a is the unit normal vector $n_a = -\alpha \nabla_a t$ to the spatial slices. Next we decompose the Faraday tensor as

$$F^{ab} = n^a E^b - n^b E^a + \epsilon^{abc} B_c \quad (63)$$

so that E^a and B^a are the electric and magnetic fields observed by a normal observer n^a . Both fields are purely spatial, i.e.

$$E^a n_a = 0 = B^a n_a. \quad (64)$$

The three-dimensional Levi-Civita tensor is defined by

$$\epsilon^{abc} = \epsilon^{abcd} n_d, \quad (65)$$

$$\epsilon^{abcd} = -\frac{1}{\sqrt{-g}} [a b c d], \quad (66)$$

where $[a b c d]$ is the antisymmetrization symbol. We also decompose the current four-vector \mathcal{J}^a as

$$\mathcal{J}^a = n^a \rho_e + J^a, \quad (67)$$

where ρ_e and J^a are the charge and current density as observed by a normal observer n^a . Note that J^a is purely spatial.

With these definitions, Maxwell's equations $\nabla_b F^{ab} = 4\pi \mathcal{J}^a$ and $\nabla_{[a} F_{bc]} = 0$ take the following 3+1 form:

$$D_i E^i = 4\pi \rho_e, \quad (68)$$

$$\partial_t E^i = \epsilon^{ijk} D_j (\alpha B_k) - 4\pi \alpha J^i + \alpha K E^i + \mathcal{L}_\beta E^i, \quad (69)$$

$$D_i B^i = 0, \quad (70)$$

$$\partial_t B^i = -\epsilon^{ijk} D_j (\alpha E_k) + \alpha K B^i + \mathcal{L}_\beta B^i, \quad (71)$$

where K is the trace of the extrinsic curvature, D_i is the covariant derivative compatible with γ_{ij} , and \mathcal{L} denotes a Lie derivative.

It follows from $\nabla_{[a} F_{bc]} = 0$ that F_{ab} can be expressed in terms of a vector potential

$$F_{ab} = \partial_a \mathcal{A}_b - \partial_b \mathcal{A}_a. \quad (72)$$

We decompose \mathcal{A}_a according to

$$\mathcal{A}_a = \Phi_e n_a + A_a, \quad (73)$$

where the three-vector potential A^a as observed by a normal observer n^a is purely spatial ($A^a n_a = 0$). The relationship between Φ_e , A_k , E^i and B^j are given by

$$\partial_t A_i = -\alpha E_i - \partial_i (\alpha \Phi_e) + \mathcal{L}_\beta A_i, \quad (74)$$

$$B^i = \epsilon^{ijk} A_{k,j}. \quad (75)$$

In the ideal MHD limit, the fluid is assumed to have perfect conductivity, which is equivalent to the condition that the electric field vanish in the fluid's rest frame. The relation between the electric and magnetic field is given by

$$\alpha E_i = -\epsilon_{ijk} (v^j + \beta^j) B^k, \quad (76)$$

where $v^j = u^j/u^t$. In the Newtonian limit, the above equation reduces to the familiar form $\mathbf{E} = -\mathbf{v} \times \mathbf{B}$.

In the ideal MHD limit, the Faraday's law (71) becomes

$$\partial_t \mathcal{B}^i = \partial_j (v^i \mathcal{B}^j - v^j \mathcal{B}^i), \quad (77)$$

where $\mathcal{B}^i = \sqrt{\gamma} B^i$. Here γ is the determinant of the spatial metric γ_{ij} . Equation (77) is the relativistic version of Eq. (6).

To derive the relativistic Navier-Stokes equation in the ideal MHD limit, we separate the stress-energy tensor into a fluid part and an electromagnetic part:

$$T^{ab} = T_{\text{fluid}}^{ab} + T_{\text{em}}^{ab}, \quad (78)$$

where

$$T_{\text{fluid}}^{ab} = T_{\text{p}}^{ab} + T_{\text{vis}}^{ab} \quad (79)$$

$$T_{\text{p}}^{ab} = \rho h u^a u^b + P g^{ab} \quad (80)$$

$$T_{\text{em}}^{ab} = \frac{1}{4\pi} \left(F^{ac} F^b{}_c - \frac{1}{4} g^{ab} F_{cd} F^{cd} \right). \quad (81)$$

Here $h = 1 + \epsilon + P/\rho$ is the specific enthalpy, $\rho\epsilon$ is the internal energy density, and T_{p}^{ab} is the stress-energy tensor for a perfect fluid. An incompressible fluid may be regarded as a gamma-law equation of state $P = (\Gamma - 1)\rho\epsilon$ in the limit $\Gamma \rightarrow \infty$. Hence we have $\epsilon = 0$ for an incompressible fluid. The viscous stress-energy tensor T_{vis}^{ab} is given by [see, e.g. [60], Eq. (22.16a)]

$$T_{\text{vis}}^{ab} = -2\eta\sigma^{ab} - \zeta P^{ab} \nabla_c u^c. \quad (82)$$

The projection tensor P^{ab} and the shear tensor σ^{ab} are defined as

$$P^{ab} = g^{ab} + u^a u^b \quad (83)$$

$$\sigma^{ab} = \frac{1}{2} (\nabla_c u^a P^{cb} + \nabla_c u^b P^{ca}) - \frac{1}{3} P^{ab} \nabla_c u^c. \quad (84)$$

For an incompressible fluid, $\nabla_c u^c = 0$. The relativistic Navier-Stokes equation is computed from the spatial components of the equation $\nabla_a T^{ab} = 0$. The result is

$$\begin{aligned} \partial_t (\sqrt{\gamma} S_i) + \partial_j (\sqrt{\gamma} S_i v^j) &= -\alpha \sqrt{\gamma} \left(\partial_i P + \frac{S_a S_b}{2\alpha S^t} \partial_i g^{ab} \right) \\ &+ \alpha \sqrt{\gamma} F_{ia} \mathcal{J}^a + 2\partial_b (\alpha \sqrt{\gamma} \eta \sigma_i^b) + \eta \sigma_{bc} \partial_i g^{bc}, \end{aligned} \quad (85)$$

where

$$S_a = \rho h \alpha u^t u_a. \quad (86)$$

Lorentz's force law implies

$$4\pi \mathcal{J}^a = \nabla_b F^{ab} = \frac{1}{\sqrt{-g}} \partial_b (\sqrt{-g} F^{ab}). \quad (87)$$

Hence we have

$$\alpha \sqrt{\gamma} F_{ia} \mathcal{J}^a = \frac{1}{4\pi} F_{ia} \partial_b (\alpha \sqrt{\gamma} F^{ab}). \quad (88)$$

Equations (85) and (88) comprise the relativistic version of Eq. (7).

B. Basic Equations

The metric for a uniform density, spherical star is given by (see, e.g. [60], Box 23.2)

$$ds^2 = -\alpha^2(r) dt^2 + \frac{dr^2}{\lambda^2(r)} + r^2 (d\theta^2 + \sin^2 \theta d\phi^2), \quad (89)$$

where

$$\alpha(r) = \begin{cases} \frac{3}{2} \sqrt{1 - \frac{2M}{R}} - \frac{1}{2} \sqrt{1 - \frac{2Mr^2}{R^3}} & (r \leq R) \\ \sqrt{1 - \frac{2M}{r}} & (r \geq R) \end{cases}, \quad (90)$$

and

$$\lambda(r) = \begin{cases} \sqrt{1 - \frac{2Mr^2}{R^3}} & (r \leq R) \\ \sqrt{1 - \frac{2M}{r}} & (r \geq R) \end{cases}. \quad (91)$$

The interior pressure is

$$P(r) = \frac{\lambda(r) - \alpha_R}{3\alpha_R - \lambda(r)} \rho, \quad (92)$$

where

$$\alpha_R = \alpha(r = R) = \sqrt{1 - \frac{2M}{R}}. \quad (93)$$

In the presence of slow rotation, small magnetic field and viscosity, the diagonal components of the background metric has a correction of order Ω^2 , $|\mathbf{B}|^2$ and $\eta|\nabla\Omega|$, which will be neglected since they are of higher nonlinear order. Rotation induces the off-diagonal component $g_{t\phi}$, which corresponds to the dragging of inertia frames. We write

$$g_{t\phi} = \beta_\phi = -r^2 \sin^2 \theta \omega(r, \theta), \quad (94)$$

where $\omega(r, \theta)$ is the angular frequency of the zero angular momentum observer (ZAMO) observed by an inertial observer at infinity. In order of magnitude, $\omega/\Omega \sim M/R$. We adopt the Cowling approximation, which assumes that the background metric is fixed, i.e. $\partial_t g_{\mu\nu} = 0$. We can justify this approximation by the following argument. First, we can use the gauge degrees of freedom to freeze the lapse and shift: $\partial_t \alpha = \partial_t \beta_i = 0$. Second, the evolution of the spatial metric γ_{ij} is given by the ADM equations [69]

$$\partial_t \gamma_{ij} = -2\alpha K_{ij} + D_i \beta_j + D_j \beta_i, \quad (95)$$

$$\begin{aligned} \partial_t K_{ij} &= -D_i D_j \alpha + \alpha (R_{ij} - 2K_{ik} K^k{}_j + K K_{ij}) \\ &- 8\pi \alpha \left[S_{ij} - \frac{1}{2} \gamma_{ij} (S - \rho_s) \right] + \beta^k D_k K_{ij} \\ &+ K_{ik} D_j \beta^k + K_{kj} D_i \beta^k, \end{aligned} \quad (96)$$

where K_{ij} is the extrinsic curvature, R_{ij} is the three-dimensional Ricci tensor, $K = K^j{}_j$, and

$$\rho_s = n_\mu n_\nu T^{\mu\nu}, \quad (97)$$

$$S_{ij} = \gamma_{ik} \gamma_{jm} T^{km}, \quad S = S^j{}_j, \quad (98)$$

where $T^{\mu\nu}$ is the total stress-energy tensor. We assume that the star is in hydrostatic quasi-equilibrium at $t = 0$. The time derivatives $\partial_t \gamma_{ij}$ and $\partial_t K_{ij}$ come from the changes in the matter and B -field sources term $\delta\rho_s$, δS_{ij} and δS , which are all of the order Ω^2 , $|\mathbf{B}|^2$ and $\eta|\nabla\Omega|$. This means that the deviation of γ_{ij} from its initial value will remain higher order. Hence our gauge conditions does not introduce a first order correction to the spatial metric in later times, and the Cowling approximation is valid.

As in the Newtonian case, we assume that the system is axisymmetric and $v^r(t; r, \theta) = v^\theta(t; r, \theta) = 0$, $v^\phi(t; r, \theta) = \Omega(t; r, \theta)$, $B^\phi(0; r, \theta) = 0$. It follows from Eq. (77) that $\partial_t B^r = \partial_t B^\theta = 0$. Hence the poloidal field remains unchanged, just like the Newtonian case. Denote the initial magnetic field

$$\mathbf{B}(0; r, \theta) = B^r(0; r, \theta)\mathbf{e}_r + B^\theta(0; r, \theta)\mathbf{e}_\theta, \quad (99)$$

where $\mathbf{e}_r = \partial/\partial r$ and $\mathbf{e}_\theta = \partial/\partial\theta$. Taking the ϕ -component of Eq. (77), we have

$$\begin{aligned} \partial_t B^\phi &= \frac{1}{\sqrt{\gamma}} \partial_j (\Omega \sqrt{\gamma} B^j) \\ &= \Omega \frac{1}{\sqrt{\gamma}} \partial_j (\sqrt{\gamma} B^j) + B^j \partial_j \Omega \\ &= B^j(0) \partial_j \Omega, \end{aligned} \quad (100)$$

where we have used Eq. (70) to obtain the last equality.

The ϕ -components of Eqs. (85) and (88) simplify to

$$\partial_t S_\phi = \frac{1}{4\pi\sqrt{\gamma}} F_{\phi b} \partial_c (\alpha \sqrt{\gamma} F^{bc}) + 2\partial_b (\alpha \sqrt{\gamma} \eta \sigma_\phi^b). \quad (101)$$

It follows from $v^\phi = \Omega$ and $u^\alpha u_\alpha = -1$ that

$$u^t = \frac{1}{\alpha} + O(\Omega^2), \quad u^\phi = \frac{\Omega}{\alpha} + O(\Omega^3), \quad (102)$$

$$u_\phi = g_{\phi\mu} u^\mu = \frac{r^2 \sin^2 \theta}{\alpha} (\Omega - \omega) + O(\Omega^3). \quad (103)$$

Using Eq. (86), we obtain

$$S_\phi = \frac{\rho + P}{\alpha} r^2 \sin^2 \theta (\Omega - \omega) + O(\Omega^3). \quad (104)$$

Straightforward calculations from Eqs. (63) and (76) using the metric (89) yield, to the leading order,

$$\begin{aligned} F_{\phi b} \partial_c (\alpha \sqrt{\gamma} F^{bc}) &= \frac{r^2 \sin \theta}{\lambda} B^j(0) \partial_j (\alpha r^2 \sin^2 \theta B^\phi) \\ &\quad - \frac{r^4 \sin^3 \theta}{\alpha \lambda} \gamma_{ij} B^i(0) B^j(0) \partial_t \Omega, \end{aligned} \quad (105)$$

where we have imposed our gauge condition $\partial_t \beta_i = 0$ by dropping a term involving $\partial_t \omega$. The viscosity term is [from Eq. (84)]

$$\begin{aligned} 2\partial_b (\alpha \sqrt{\gamma} \eta \sigma_\phi^b) &= \partial_r (\eta \lambda r^4 \sin^3 \theta \partial_r \Omega) + \partial_\theta \left(\eta \frac{r^2 \sin^3 \theta}{\lambda} \partial_\theta \Omega \right) \\ &\quad + O(\eta \Omega^2). \end{aligned} \quad (106)$$

Gathering all the terms, we obtain

$$\begin{aligned} \left[1 + \frac{\gamma_{ij} B^i(0) B^j(0)}{4\pi(\rho + P)} \right] \partial_t \Omega &= \frac{\alpha B^j(0) \partial_j (\alpha r^2 \sin^2 \theta B^\phi)}{4\pi(\rho + P) r^2 \sin^2 \theta} \\ &\quad + \frac{\alpha \lambda}{(\rho + P) r^4 \sin^3 \theta} [\partial_r (\eta r^4 \lambda \sin^3 \theta \partial_r \Omega) \\ &\quad + \partial_\theta \left(\eta \frac{r^2 \sin^3 \theta}{\lambda} \partial_\theta \Omega \right)] \end{aligned} \quad (107)$$

The term on the left-hand side, $\gamma_{ij} B^i(0) B^j(0)/4\pi(\rho + P) \sim v_A^2 \sim E_{\text{mag}}/M$, is assumed to be small. Hence it can be neglected. We also note that to the leading order in our adopted gauge, the frame dragging frequency ω does not enter into the evolution equations. It follows from Eq. (92) that

$$\rho + P(r) = \rho \frac{\alpha_R}{\alpha(r)}. \quad (108)$$

Combining the results, we obtain the relativistic version of Eqs. (16) and (17):

$$\partial_t B^\phi = B^j(0) \partial_j \Omega \quad (109)$$

$$\begin{aligned} \partial_t \Omega &= \frac{\alpha^2}{\alpha_R} \frac{1}{4\pi \rho r^2 \sin^2 \theta} B^j(0) \partial_j (\alpha r^2 \sin^2 \theta B^\phi) \\ &\quad + (\partial_t \Omega)_{\text{vis}}, \end{aligned} \quad (110)$$

where

$$(\partial_t \Omega)_{\text{vis}} = \frac{\alpha^2 \lambda}{\alpha_R} \left[\frac{1}{r^4} \partial_r (\nu \lambda r^4 \partial_r \Omega) + \frac{1}{\lambda r^2 \sin^3 \theta} \partial_\theta (\nu \sin^3 \theta \partial_\theta \Omega) \right]. \quad (111)$$

Here we again set $\nu = \eta/\rho$. The condition that the toroidal field cannot be carried outside the star gives the boundary conditions $B^\phi = 0$ at $r = R$, which also implies [from Eq. (109)] $B^j(0) \partial_j \Omega = 0$ at $r = R$. In the Newtonian limit, with $M/R \ll 1$, Eqs. (109)–(111) reduce to the Newtonian MHD equations (16)–(18).

C. Initial Magnetic Field

The two sets of poloidal field functions we discussed in Section III B cannot be used in the relativistic case because they do not satisfy the relativistic Maxwell equation $D_i B^i(0) = 0$. We want to choose two sets of initial field which will reduce to the ones we discussed in Section III B in the Newtonian limit. It is easy to prove that any axisymmetric poloidal field can be generated by a vector potential of the form $A_i = A_\phi \delta_i^\phi$. Hence we can specify A_ϕ and then compute $B^j(0)$ from Eq. (75). This guarantees that the constraint equation $D_i B^i(0) = 0$ is satisfied.

The simplest way to generalize the Newtonian initial fields is to use the same A_ϕ as in the Newtonian cases [Eqs. (24) and (25)]. Hence the “ $l = 1$ ” field is generated by

$$A_\phi = \frac{1}{2}B_0 r^2 \sin^2 \theta . \quad (112)$$

The corresponding poloidal field is given by Eq. (75), yielding

$$B^r = \lambda B_0 \cos \theta , \quad B^\theta = -\lambda \frac{B_0}{r} \sin \theta . \quad (113)$$

We define cylindrical coordinates $\varpi = r \sin \theta$, $z = r \cos \theta$. The cylindrical components of the poloidal field are

$$B^\varpi = 0 , \quad B^z = \lambda B_0 . \quad (114)$$

We see that the poloidal field is still in the z direction. However, its amplitude

$$\begin{aligned} |\mathbf{B}(0)| &= \sqrt{\gamma_{ij} B^i(0) B^j(0)} \\ &= B_0 \sqrt{1 - \frac{2M\varpi^2}{R^3}} \end{aligned} \quad (115)$$

decreases with increasing ϖ .

The generalized “ $l = 2$ ” field is generated by

$$A_\phi = B_0 \frac{r^3}{R} \sin^2 \theta \cos \theta . \quad (116)$$

The poloidal field has components

$$B^r = \lambda B_0 \frac{r}{R} (3 \cos^2 \theta - 1) , \quad B^\theta = -\frac{3\lambda B_0}{R} \sin \theta \cos \theta . \quad (117)$$

It follows that the shape of the field line of this $l = 2$ field is the same as the Newtonian $l = 2$ field shown in Fig. 1, even though the magnitude is different.

D. Conserved Integrals

As in the Newtonian case, the relativistic MHD equations (109) and (110) admit two non-trivial integrals of motion, expressing the conservation of energy and angular momentum. The derivation is very similar to the Newtonian case, so we just state the result here.

The conserved energy contains a sum of three terms:

$$E = E_{\text{rot}} + E_{\text{mag}} + E_{\text{vis}} , \quad (118)$$

where

$$E_{\text{rot}} = \frac{1}{2} \int \left(\frac{\rho + P}{\alpha} \Omega^2 r^2 \sin^2 \theta \right) \frac{r^2 \sin \theta}{\lambda} dr d\theta d\phi , \quad (119)$$

$$E_{\text{mag}} = \int \alpha \frac{(B^\phi)^2}{8\pi} \frac{r^2 \sin \theta}{\lambda} dr d\theta d\phi , \quad (120)$$

$$E_{\text{vis}} = \int_0^t \dot{E}_{\text{vis}}(t') dt' , \quad (121)$$

and where

$$\dot{E}_{\text{vis}} = \int \eta r^2 \sin^2 \theta \left[\lambda^2 (\partial_r \Omega)^2 + \frac{(\partial_\theta \Omega)^2}{r^2} \right] \frac{r^2 \sin \theta}{\lambda} dr d\theta d\phi \quad (122)$$

$$= \int \eta r^2 \sin^2 \theta g^{ij} \nabla_i \Omega \nabla_j \Omega \frac{r^2 \sin \theta}{\lambda} dr d\theta d\phi . \quad (123)$$

The conserved angular momentum is

$$J = \int \frac{\rho + P}{\alpha} (\Omega r^2 \sin^2 \theta) \frac{r^2 \sin \theta}{\lambda} dr d\theta d\phi . \quad (124)$$

E. Special Coordinates and Phase Mixing

As in the Newtonian case, in the absence of viscosity, Eqs. (109) and (110) can be brought into 1+1 form by the coordinate transformation $u = u(r, \theta)$, $v = v(r, \theta)$ that satisfies

$$B^j(0) \frac{\partial u}{\partial x^j} = \kappa(u, v) , \quad (125)$$

$$B^j(0) \frac{\partial v}{\partial x^j} = 0 . \quad (126)$$

In these new coordinates, Eqs (109) and (110) become (without viscosity)

$$\partial_t B^\phi = \kappa \partial_u \Omega \quad (127)$$

$$\partial_t \Omega = \frac{\alpha^2}{\alpha_R} \frac{\kappa}{4\pi \rho r^2 \sin^2 \theta} \partial_u (\alpha r^2 \sin^2 \theta B^\phi) . \quad (128)$$

It follows from Eq. (75) that when $A_i = A_\phi \delta_i^\phi$,

$$B^r = \frac{1}{\sqrt{\gamma}} \partial_\theta A_\phi , \quad B^\theta = -\frac{1}{\sqrt{\gamma}} \partial_r A_\phi . \quad (129)$$

Hence we have $B^i \partial_i A_\phi = 0$. We can choose $v = f(A_\phi)$ as in the Newtonian case, where f is an arbitrary function with continuous first derivative. Since we use the same A_ϕ as the Newtonian case in constructing the initial magnetic field, we can use the same u and v to simplify the MHD equations.

In particular, we use cylindrical coordinates defined by $\varpi = r \sin \theta$ and $z = r \cos \theta$ for the $l = 1$ field. In these coordinates, the MHD equations become

$$\partial_t B^\phi = \lambda B_0 \partial_z \Omega \quad (130)$$

$$\partial_t \Omega = \frac{\alpha^2 \lambda}{\alpha_R} \left(\frac{B_0}{4\pi \rho} \right) \partial_z (\alpha B^\phi) . \quad (131)$$

For the $l = 2$ field, we choose

$$u = -r^2 (3 \cos^2 \theta - 1) , \quad (132)$$

$$v = r^3 \sin^2 \theta \cos \theta . \quad (133)$$

It follows from Eq. (125) that

$$\kappa = B^j(0) \partial_j u = -\frac{2\lambda B_0 r^2}{R} (3 \cos^2 \theta + 1) . \quad (134)$$

The MHD equations become

$$\partial_t B^\phi = -\frac{2\lambda B_0 r^2}{R}(3\cos^2\theta + 1)\partial_u \Omega \quad (135)$$

$$\begin{aligned} \partial_t \Omega = & -\left(\frac{\alpha^2 \lambda}{\alpha_R}\right) \frac{2B_0}{4\pi\rho R} [r^2(3\cos^2\theta + 1)\partial_u(\alpha B^\phi) \\ & + \alpha B^\phi] . \end{aligned} \quad (136)$$

Here r and θ are regarded as implicit functions of u and v .

As discussed in Section III D, Eqs. (127) and (128) imply that there is no coupling of B^ϕ and Ω between different poloidal field lines. The toroidal field and angular velocity will oscillate in general at different characteristic frequencies along different field lines. The angular velocity flow and toroidal field pattern will become irregular as a result. We will demonstrate this phase mixing effect in Section VI when we present our numerical results.

V. NONDIMENSIONAL FORMULATION

Before numerically integrating the MHD equations, it is convenient to introduce the following nondimensional variables:

$$\hat{r} = \frac{r}{R}, \quad (137)$$

$$\hat{t} = \frac{B_0 t}{R\sqrt{4\pi\rho}} = \frac{t}{t_A}, \quad (138)$$

$$\hat{B} = \frac{\alpha B^\phi}{\Omega_c \sqrt{4\pi\rho}} = \frac{\alpha B^\phi}{\Omega_c r \sin\theta \sqrt{4\pi\rho}}, \quad (139)$$

$$\hat{B}^j(0) = \frac{B^j(0)}{B_0}, \quad j = r, \theta, \quad (140)$$

$$\hat{\Omega} = \frac{\Omega}{\Omega_c}, \quad (141)$$

$$\hat{v} = \frac{\nu}{R} \left(\frac{\sqrt{4\pi\rho}}{B_0} \right), \quad (142)$$

$$\hat{E} = \frac{E}{M(R\Omega_c)^2}, \quad (143)$$

$$\hat{J} = \frac{J}{MR^2\Omega_c}, \quad (144)$$

where the Alfvén time t_A is defined as

$$t_A = \frac{R}{B_0/\sqrt{4\pi\rho}}. \quad (145)$$

Here Ω_c is an arbitrary constant with a magnitude characteristic of the initial angular velocity. In terms of these new variables, Eqs. (109) and (110) become

$$\partial_{\hat{t}} \hat{B} = \alpha \hat{B}^j(0) \partial_j \hat{\Omega} \quad (146)$$

$$\partial_{\hat{t}} \hat{\Omega} = \frac{\alpha^2}{\alpha_R} \frac{\hat{B}^j(0)}{\hat{r}^2 \sin^2\theta} \partial_j (\hat{r}^2 \sin^2\theta \hat{B}) + (\partial_{\hat{t}} \hat{\Omega})_{\text{vis}}, \quad (147)$$

where $\partial_j = R\partial_j$ and

$$\begin{aligned} (\partial_{\hat{t}} \hat{\Omega})_{\text{vis}} = & \frac{\alpha^2 \lambda}{\alpha_R \hat{r}^4 \sin^3\theta} \left[\partial_{\hat{r}} (\hat{v} \hat{r}^4 \sin^3\theta \partial_{\hat{r}} \hat{\Omega}) \right. \\ & \left. + \partial_{\theta} \left(\hat{v} \frac{\hat{r}^2 \sin^3\theta}{\lambda} \partial_{\theta} \hat{\Omega} \right) \right]. \end{aligned} \quad (148)$$

Since the background pressure distribution is spherical, it is reasonable to assume that $\nu = \nu(r)$, hence

$$\begin{aligned} (\partial_{\hat{t}} \hat{\Omega})_{\text{vis}} = & \frac{\alpha \lambda}{\alpha_R} \left\{ \hat{v} \lambda \partial_{\hat{r}}^2 \hat{\Omega} + \left[\partial_{\hat{r}}(\nu \lambda) + \frac{4}{\hat{r}} \nu \lambda \right] \partial_{\hat{r}} \hat{\Omega} \right. \\ & \left. + \frac{\hat{v}}{\lambda \hat{r}^2} (\partial_{\theta}^2 \hat{\Omega} + 3 \cot\theta \partial_{\theta} \hat{\Omega}) \right\}. \end{aligned} \quad (149)$$

The Navier-Stokes equation and the regularity condition on the surface of the star require that the dynamic viscosity η in general has to decrease to zero continuously as the surface of the star is approached. We adopt the simplest viscosity model in our numerical computations: we assume that $\nu = \eta/\rho$ is essentially constant in the interior, but rapidly drops to zero when approaching the surface of the star at $r = R$.

While the variable \hat{B} is convenient for numerical evolution of the MHD equations, we also found it convenient to introduce another non-dimensional variable

$$\bar{B} = \frac{\hat{r} \sin\theta}{\alpha} \hat{B} = \left(\frac{B^\phi}{B_0} \right) \left(\frac{v_A}{\Omega_c R} \right), \quad (150)$$

which is a measure of the strength of the toroidal magnetic field. Note that in this non-dimensional formulation, we do not need to specify the ratio $v_A/\Omega_c R$, which is assumed to be much greater than one so that $E_{\text{mag}} \gg E_{\text{rot}}$. We also do not need to specify the characteristic amplitude of the seed poloidal magnetic field B_0 , which has to be small so that $E_{\text{mag}} \ll W$ or equivalently, $v_A \ll 1$. These quantities are absorbed in our nondimensional variables.

In the next two subsections, we will further simplify the general equations above by inserting the specific forms of the two sets of initial magnetic field.

A. Equations for the $l = 1$ Field

As discussed in Sections III D and IV E, the cylindrical coordinates $\hat{\omega} = \hat{r} \sin\theta$ and $\hat{z} = \hat{r} \cos\theta$ are the preferred coordinates in the absence of viscosity. To impose the boundary condition at $\hat{r} = 1$, it is convenient to introduce a new variable $\hat{u} = \hat{z}/\sqrt{1 - \hat{\omega}^2}$ in place of \hat{z} . The boundary of the star is located at $\hat{u} = 1$. We are interested in a solution in which Ω is symmetric under the reflection $z \rightarrow -z$. Hence the computation domain is $\hat{u} \in [0, 1]$ and $\hat{\omega} \in [0, 1]$. The MHD equations, in terms of \hat{u} and $\hat{\omega}$, take the form

$$\partial_{\hat{t}} \hat{B} = \frac{\alpha \lambda}{\sqrt{1 - \hat{\omega}^2}} \partial_{\hat{u}} \hat{\Omega} \quad (151)$$

$$\partial_{\hat{t}}\hat{\Omega} = \frac{\alpha^2\lambda}{\alpha_R\sqrt{1-\hat{\omega}^2}}\partial_{\hat{u}}\hat{B} + (\partial_{\hat{t}}\hat{\Omega})_{\text{vis}}, \quad (152)$$

where $(\partial_{\hat{t}}\hat{\Omega})_{\text{vis}}$ is obtained from Eq. (149) and Eqs. (C7)–(C10).

The nondimensional energy and angular momentum are given by

$$\hat{J} = 3\alpha_R \int_0^1 d\hat{\omega} \hat{\omega}^3 \sqrt{1-\hat{\omega}^2} \int_0^1 d\hat{u} \frac{\hat{\Omega}}{\alpha^2\lambda} \quad (153)$$

$$\hat{E} = \hat{E}_{\text{rot}}(\hat{t}) + \hat{E}_{\text{mag}}(\hat{t}) + \int_0^{\hat{t}} dt' \dot{\hat{E}}_{\text{vis}}(t'), \quad (154)$$

where

$$\hat{E}_{\text{rot}} = \frac{3}{2} \int_0^1 d\hat{\omega} \hat{\omega}^3 \sqrt{1-\hat{\omega}^2} \hat{\epsilon}_1^{\text{rot}}(\hat{\omega}), \quad (155)$$

$$\hat{E}_{\text{mag}} = \frac{3}{2} \int_0^1 d\hat{\omega} \hat{\omega}^3 \sqrt{1-\hat{\omega}^2} \hat{\epsilon}_1^{\text{mag}}(\hat{\omega}) \quad (156)$$

$$\dot{\hat{E}}_{\text{vis}} = -3 \int_0^1 d\hat{\omega} \int_0^1 d\hat{z} \frac{\hat{\omega}^3 \hat{\nu}}{\lambda} \left[\lambda^2 (\partial_{\hat{r}}\hat{\Omega})^2 + \frac{(\partial_{\theta}\hat{\Omega})^2}{\hat{r}^2} \right] \quad (157)$$

The functions $\hat{\epsilon}_1^{\text{rot}}(\hat{\omega})$ and $\hat{\epsilon}_1^{\text{mag}}(\hat{\omega})$ are given by

$$\hat{\epsilon}_1^{\text{rot}}(\hat{\omega}) = \int_0^1 d\hat{u} \frac{\alpha_R}{\alpha^2\lambda} \hat{\Omega}^2, \quad (158)$$

$$\hat{\epsilon}_1^{\text{mag}}(\hat{\omega}) = \int_0^1 d\hat{u} \frac{\hat{B}^2}{\alpha\lambda}. \quad (159)$$

In the absence of viscosity, there is no coupling between different values of $\hat{\omega}$. Hence the reduced energy and angular momentum functions

$$\hat{\epsilon}_1(\hat{\omega}) = \hat{\epsilon}_1^{\text{rot}}(\hat{\omega}) + \hat{\epsilon}_1^{\text{mag}}(\hat{\omega}), \quad (160)$$

$$\hat{j}_1(\hat{\omega}) = \int_0^1 d\hat{u} \frac{\hat{\Omega}}{\alpha^2\lambda} \quad (161)$$

are also conserved for each value of $\hat{\omega}$. This can also be proved directly from Eqs. (151) and (152).

B. Equations for the $l = 2$ Field

In the absence of viscosity, the preferred coordinates are $u = -r^2(3\cos^2\theta - 1)$ and $v = r^3\sin^2\theta\cos\theta$. In numerical calculations, it is more convenient to introduce the following nondimensional variables

$$\hat{u} = \frac{u - u_1(v)}{u_2(v) - u_1(v)} \quad (162)$$

$$\hat{v} = \frac{3\sqrt{3}}{2} \hat{r}^3 \sin^2\theta \cos\theta, \quad (163)$$

where $u_1(v)$ and $u_2(v)$ are the values of u at which a given $v=\text{constant}$ line intercepts the sphere $r = R$, the surface of the star, with $u_2 > u_1$ (see Fig. 2).

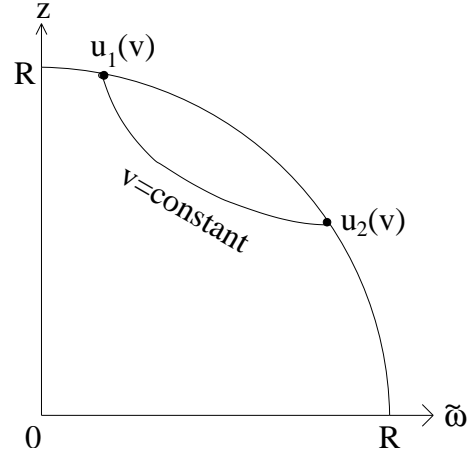


FIG. 2: The points $u_1(v)$ and $u_2(v)$.

The MHD equations, in terms of \hat{u} and \hat{v} , take the form

$$\partial_{\hat{t}}\hat{B} = -\frac{2\alpha\lambda r^2(3\cos^2\theta + 1)}{u_2(v) - u_1(v)}\partial_{\hat{u}}\hat{\Omega} \quad (164)$$

$$\partial_{\hat{t}}\hat{\Omega} = -\frac{2\alpha^2\lambda}{\alpha_R} \left[\frac{r^2(3\cos^2\theta + 1)}{u_2(v) - u_1(v)}\partial_{\hat{u}}\hat{B} + \hat{B} \right] + (\partial_{\hat{t}}\hat{\Omega})_{\text{vis}}. \quad (165)$$

Note that the relativistic factors α and λ are functions of r . The variables r and θ are regarded as implicit functions of \hat{u} and \hat{v} . The transformation between these two sets of variables are derived in Appendix B. we only consider the solution with equatorial symmetry. The computation domain is $\hat{u} \in [0, 1]$ and $\hat{v} \in [0, 1]$. The boundary of the star is located at $\hat{u} = 0$ and $\hat{u} = 1$. As in the Newtonian case, lines of constant \hat{v} coincide with poloidal field lines.

It is not easy to handle the viscosity term $(\partial_{\hat{t}}\hat{\Omega})_{\text{vis}}$ numerically in this (\hat{u}, \hat{v}) coordinate system because of the coordinate singularity at $\hat{v} = 0$ and $\hat{v} = 1$. Besides, these particular coordinates lose their advantage in the presence of viscosity. Hence we use the cylindrical-like coordinates introduced in Section V A when we study the effect of viscosity.

In the absence of viscosity, the energy \hat{E} and angular momentum \hat{J} are given by

$$\hat{E} = \frac{1}{2\sqrt{3}} \int_0^1 d\hat{v} \frac{u_2(v) - u_1(v)}{R^2} \hat{\epsilon}_2(\hat{v}) \quad (166)$$

$$\hat{J} = \frac{\alpha_R}{\sqrt{3}} \int_0^1 d\hat{v} \frac{u_2(v) - u_1(v)}{R^2} \hat{j}_2(\hat{v}), \quad (167)$$

where

$$\hat{\epsilon}_2(\hat{v}) = \hat{\epsilon}_2^{\text{rot}}(\hat{v}) + \hat{\epsilon}_2^{\text{mag}}(\hat{v}), \quad (168)$$

$$\hat{\epsilon}_2^{\text{rot}}(\hat{v}) = \int_0^1 d\hat{u} \frac{\alpha_R \sin^2\theta}{\alpha^2\lambda(3\cos^2\theta + 1)} \hat{\Omega}^2, \quad (169)$$

TABLE I: Summary of the cases we have studied.

| Case | Gravitation | M/R | Poloidal field | Viscosity $\hat{\nu}$ |
|------|-------------|---------|----------------|-----------------------|
| Ia | Newtonian | $\ll 1$ | $l = 1$ | 0 |
| Ib | GR | 0.3 | $l = 1$ | 0 |
| Ic | GR | 0.44 | $l = 1$ | 0 |
| IIa | Newtonian | $\ll 1$ | $l = 2$ | 0 |
| IIb | GR | 0.3 | $l = 2$ | 0 |
| IIc | GR | 0.44 | $l = 2$ | 0 |
| III | GR | 0.3 | $l = 2$ | 0.002 |

$$\hat{\epsilon}_2^{\text{mag}}(\hat{\nu}) = \int_0^1 d\hat{u} \frac{\sin^2 \theta}{\alpha \lambda (3 \cos^2 \theta + 1)} \hat{B}^2, \quad (170)$$

$$\hat{j}_2(\hat{\nu}) = \int_0^1 d\hat{u} \frac{\Omega \sin^2 \theta}{\alpha^2 \lambda (3 \cos^2 \theta + 1)}. \quad (171)$$

It follows from Eqs. (164) and (165) that in the absence of viscosity, the functions $\hat{\epsilon}_2(\hat{\nu})$ and $\hat{j}_2(\hat{\nu})$ are conserved for each $\hat{\nu}$.

VI. NUMERICAL RESULTS

We numerically integrate the two sets of differential equations (151), (152) and (164), (165) by the iterated Crank-Nicholson method [57]. A more detailed description of our finite differencing scheme is given in Appendix C. In this section, we report our numerical results. Table I summarizes the cases we have studied.

A. Without Viscosity (Cases Ia–IIc)

In the absence of viscosity, we use the special coordinates discussed in Sections V A and V B to integrate the nondimensional MHD equations.

1. $l = 1$ initial field (Cases Ia–Ic)

As discussed in the Newtonian case, there is no magnetic braking if the initial angular velocity distribution is constant on cylinders for the $l = 1$ initial field. The same result applies for the relativistic case, as is indicated from Eq. (130). To study magnetic braking, we use the following *ad hoc* initial differential angular velocity profile[70]

$$\hat{\Omega}(0; \hat{\omega}, \hat{z}) = \frac{1}{1 + \hat{\omega}^2} - \frac{1 - \hat{\omega}^2}{2} \cos \left[\frac{\pi \hat{z}}{\sqrt{1 - \hat{\omega}^2}} \right], \quad (172)$$

which is not constant on cylinders. This corresponds to setting the function

$$C_n(\varpi) = \begin{cases} \frac{\Omega_\omega R}{2v_A} \left(1 - \frac{\varpi^2}{R^2}\right) & n = 1 \\ 0 & n > 1 \end{cases} \quad (173)$$

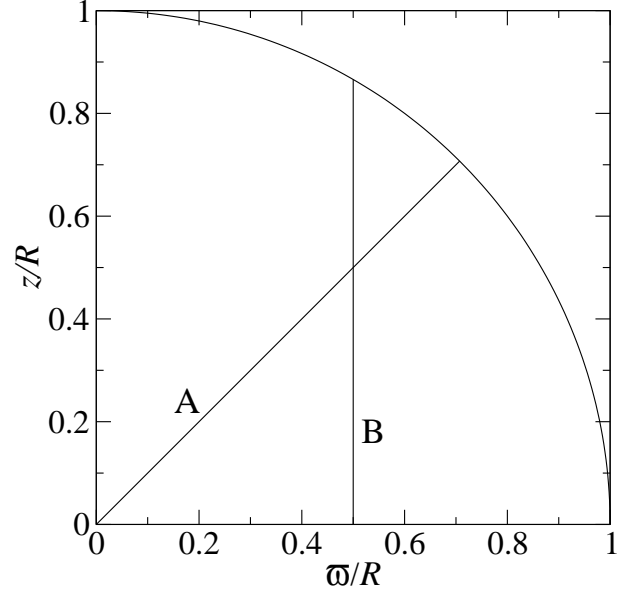


FIG. 3: The $\theta = 45^\circ$ line (line A) and $\varpi/R = 0.5$ line (line B). The circular arc is the surface of the star $r = R$.

in Eq. (58). Hence in the Newtonian limit ($M/R \ll 1$), the toroidal field and angular velocity oscillate with the fundamental eigenfrequency on each cylindrical surface, given by Eq. (57) for $n = 1$. The analytic solution in this limit is

$$\hat{\Omega}(\hat{t}; \hat{\omega}, \hat{z}) = \frac{1}{1 + \hat{\omega}^2} - \frac{1 - \hat{\omega}^2}{2} \cos \left(\frac{\pi \hat{z}}{\sqrt{1 - \hat{\omega}^2}} \right) \times \cos \left(\frac{\pi \hat{t}}{\sqrt{1 - \hat{\omega}^2}} \right), \quad (174)$$

$$\hat{B}(\hat{t}; \hat{\omega}, \hat{z}) = \frac{1 - \hat{\omega}^2}{2} \sin \left(\frac{\pi \hat{z}}{\sqrt{1 - \hat{\omega}^2}} \right) \times \sin \left(\frac{\pi \hat{t}}{\sqrt{1 - \hat{\omega}^2}} \right). \quad (175)$$

It follows from Eqs. (158)–(161) that

$$\hat{\epsilon}_1^{\text{rot}}(\hat{t}; \hat{\omega}) = \frac{1}{(1 + \hat{\omega}^2)^2} + \frac{(1 - \hat{\omega}^2)^2}{8} \times \cos^2 \left(\frac{\pi \hat{t}}{\sqrt{1 - \hat{\omega}^2}} \right), \quad (176)$$

$$\hat{\epsilon}_1^{\text{mag}}(\hat{t}; \hat{\omega}) = \frac{(1 - \hat{\omega}^2)^2}{8} \sin^2 \left(\frac{\pi \hat{t}}{\sqrt{1 - \hat{\omega}^2}} \right), \quad (177)$$

$$\hat{\epsilon}_1(\hat{\omega}) = \frac{1}{(1 + \hat{\omega}^2)^2} + \frac{(1 - \hat{\omega}^2)^2}{8}, \quad (178)$$

$$\hat{j}_1(\hat{\omega}) = \frac{1}{1 + \hat{\omega}^2}. \quad (179)$$

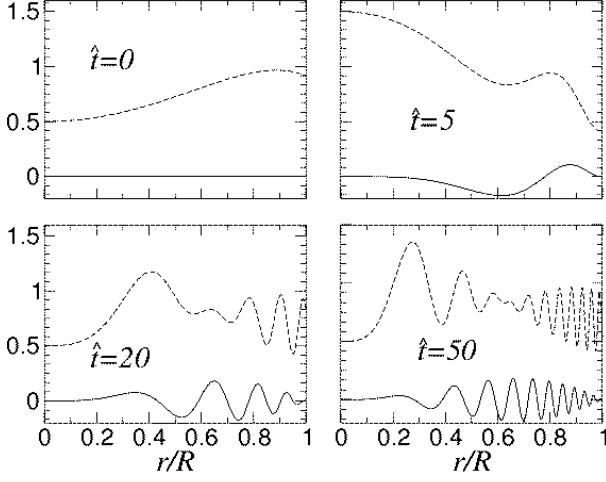


FIG. 4: Snapshots of \bar{B} (solid lines) and $\hat{\Omega}$ (dashed lines) along the $\theta = 45^\circ$ line (line A of Fig. 3) for a Newtonian star ($M/R \ll 1$). The initial magnetic field is the $l = 1$ field given by Eq. (113). As expected, small-scale structures build up at late times.

We plot the snapshots of \bar{B} and $\hat{\Omega}$ as a function of time along two arbitrary lines as shown in Fig. 3. Figure 4 shows the snapshots of \bar{B} and $\hat{\Omega}$ as a function of time along the $\theta = 45^\circ$ line based on the analytic solution given by Eqs. (174) and (175). We see that small-scale structures develop at late times, as predicted from our previous analytic study. Figure 5 shows the snapshots along the $\varpi/R = 0.5$ line. We see simple sinusoidal oscillations with a period $\hat{T} = \sqrt{3} = 1.73$. No small structure is observed since we are looking in the direction along a particular poloidal field line.

Since $\hat{j}_1(\hat{\varpi})$ is conserved, we can define a mean angular velocity for each value of $\hat{\varpi}$ by

$$\hat{\Omega}_{\text{mean}}(\hat{\varpi}) = \hat{j}_1(\hat{\varpi})/\hat{I}_1(\hat{\varpi}), \quad (180)$$

where

$$\hat{I}_1(\varpi) = \int_0^1 \frac{d\hat{u}}{\alpha^2 \lambda}. \quad (181)$$

In our Newtonian example, we have

$$\hat{\Omega}_{\text{mean}}(\hat{\varpi}) = \frac{1}{1 + \hat{\varpi}^2}. \quad (182)$$

Equation (174) indicates that for each $\hat{\varpi}$, the angular velocity $\hat{\Omega}$ oscillates about $\hat{\Omega}_{\text{mean}}$ with a period $\hat{T} = 2\sqrt{1 - \hat{\varpi}^2}$. The first term of Eq. (176) is the reduced rotational kinetic energy associated with $\hat{\Omega}_{\text{mean}}$, which is independent of time. The kinetic energy associated with the differential rotation transfers back and forth with the energy associated with the toroidal magnetic field with a period $\hat{T}/2$ (see Fig. 6).

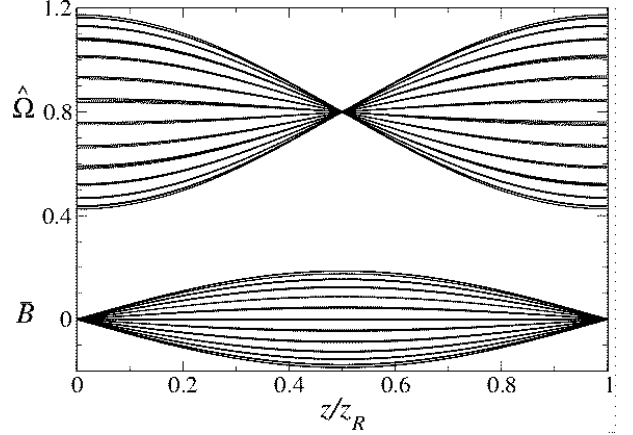


FIG. 5: Snapshots of \bar{B} (lower curves) and $\hat{\Omega}$ (upper curves) along the $\varpi/R = 0.5$ line (line B in Fig. 3) for a Newtonian star ($M/R \ll 1$). The surface of the star is located at $z = z_R = \sqrt{R^2 - \varpi^2} = R/\sqrt{2}$. Each curve represents the profile at a particular time. Both \bar{B} and $\hat{\Omega}$ oscillate sinusoidally with a period $\hat{T} = \sqrt{3} = 1.73$. Curves are plotted at time intervals $\Delta\hat{t} = 0.2$ from $\hat{t} = 0$ to $\hat{t} = 8.6$ (about 5 oscillation periods).

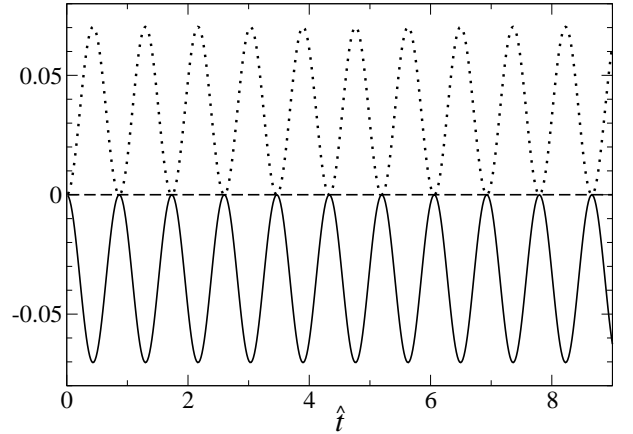


FIG. 6: Energy evolution for a differentially rotating Newtonian star with an $l = 1$ poloidal magnetic field. The solid line shows $\hat{\epsilon}_1^{\text{rot}}(\hat{t}) - \hat{\epsilon}_1^{\text{rot}}(0)$, the dotted line shows $\hat{\epsilon}_1^{\text{mag}}(\hat{t})$. The dashed line is the sum of the two lines, which is $\hat{\epsilon}_1 - \hat{\epsilon}_1^{\text{rot}}(0) = 0$. All the reduced energies are evaluated at $\hat{\varpi} = 0.5$.

There is no analytic solution to the MHD equations when the star is relativistic. We solve the MHD equations (151) and (164) numerically in this case. The appearance of small-scale structures does not cause any problem in our numerical code, because we have chosen suitable coordinates to avoid taking derivatives perpen-

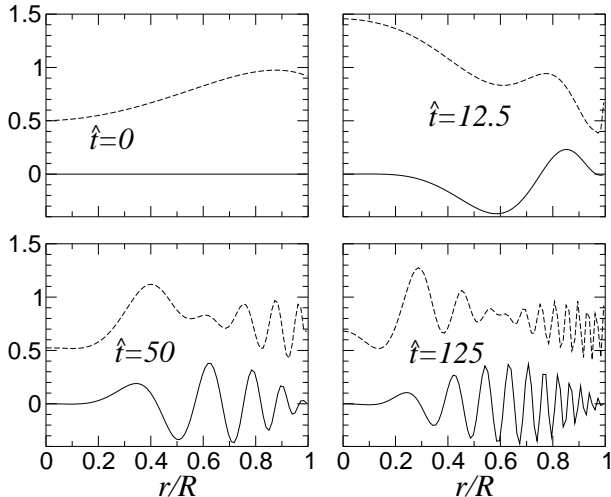


FIG. 7: Same as Fig. 4 but for a relativistic star with $M/R = 0.3$. The behavior is qualitatively the same as the Newtonian case, but the amplitude of oscillation is larger.

dicular to the poloidal field lines. To check our numerical integrations, we perform second-order convergence tests and, in addition, monitor the conserved integrals $\hat{\epsilon}_1(\hat{\omega})$ and $\hat{j}_1(\hat{\omega})$ defined in Eqs. (160) and (161). We find that the fractional change of $\hat{\epsilon}_1$ to be less than 10^{-4} from time $\hat{t} = 0$ to $\hat{t} = 100$ for various values of the compaction ratio M/R . The fractional change of \hat{j}_1 is less than 10^{-5} over the same period of time.

Figure 7 shows the snapshots of \bar{B} and $\hat{\Omega}$ for a relativistic star with $M/R = 0.3$ along the $\theta = 45^\circ$ line. We see that the behavior is qualitatively the same as the Newtonian case, but the amplitude of the toroidal field is larger by a factor of 2. Figure 8 shows the snapshots along the $\varpi/R = 0.5$ coordinate line. The initial angular velocity distribution [Eq. (172)] no longer corresponds to the fundamental mode of the relativistic equations, but it is still very close. The oscillation frequency is found to be $\hat{T} = 4.3$, which is longer than the Newtonian period by a factor of 2.5. The corresponding reduced energy is similar to Fig. 6, but the amplitudes are larger and the period is longer by a factor of 2.5 (Fig. 9). This can be understood by rewriting Eqs. (130) and (131) as

$$\partial_{\hat{t}}^2 \hat{B} = \frac{\alpha^3 \lambda^2}{\alpha_R} \left[\partial_{\hat{z}}^2 \hat{B} + \frac{\partial_{\hat{z}}(\alpha^2 \lambda)}{\alpha^2 \lambda} \hat{B} \right]. \quad (183)$$

If the background metric varies slowly along the field lines so that the term $\partial_{\hat{z}}(\alpha^2 \lambda)/\alpha^2 \lambda \ll 1$, the equation simplifies to

$$\partial_{\hat{t}}^2 \hat{B} \approx \partial_{\hat{z}}^2 \hat{B}, \quad (184)$$

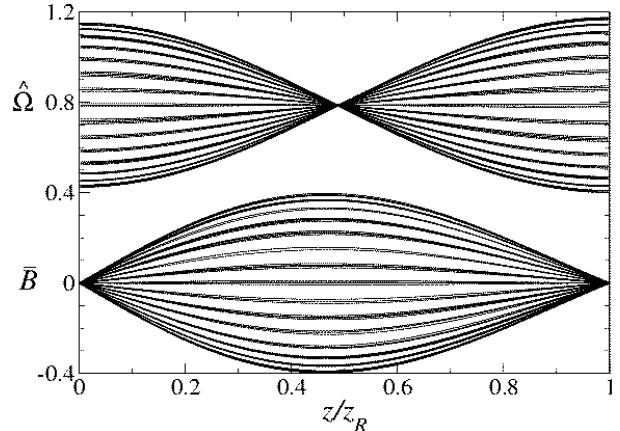


FIG. 8: Snapshots of \bar{B} (lower curves) and $\hat{\Omega}$ (upper curves) along the $\varpi/R = 0.5$ line for a relativistic star with $M/R = 0.3$. As in the Newtonian case, both \bar{B} and $\hat{\Omega}$ oscillate periodically. The oscillation period is $\hat{T} = 4.3$, which is longer than the Newtonian case because of the relativistic time dilation (see the text). Curves are plotted at time intervals $\Delta \hat{t} = 0.4$ from $\hat{t} = 0$ to $\hat{t} = 21.2$ (about 5 oscillation periods).

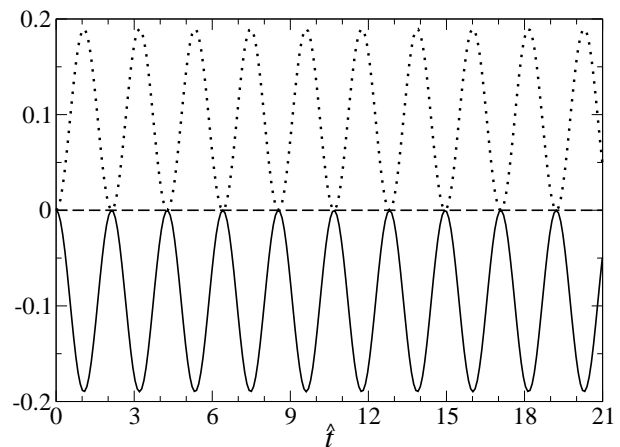


FIG. 9: Same as Fig. 6 but for a relativistic star with $M/R = 0.3$.

where

$$\hat{\tau} = \left(\frac{\alpha^3 \lambda^2}{\alpha_R} \right)^{1/2} \hat{t}. \quad (185)$$

Note that Eq. (184) does not contain explicitly the relativistic factors α and λ , which are absorbed in the new time variable $\hat{\tau}$ and \hat{B} [see Eq. (150)]. Hence in this approximation, the relativistic corrections are that (a) time is dilated according to Eq. (185), and (b) the toroidal field

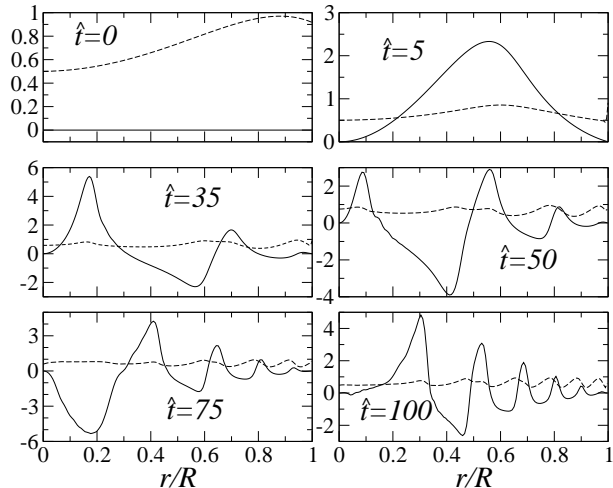


FIG. 10: Same as Fig. 4 but for a relativistic star with $M/R = 0.44$, approaching the Buchdahl limit $M/R \rightarrow 4/9$. The behavior of \bar{B} and $\hat{\Omega}$ is qualitative very different from the previous two cases. However, small-scale structure still appears at late times.

$B^{\hat{\phi}}$ is increased by a factor of $1/\alpha$ for a given initial angular velocity profile $\Omega(0; \varpi, z)$ according to Eq. (150). Following this analysis, we expect that for $M/R = 0.3$, the maximum value of \bar{B} on the $\hat{\varpi} = 0.5$ line should be about 1.9 times larger than the Newtonian value, and the oscillation period to be longer by about a factor of 2.5. Our numerical result gives a factor of 2 for the amplitude and 2.5 for the oscillation period on the cylinder $\varpi/R = 0.5$. This indicates that the background spacetime metric for this star changes slowly along the poloidal field lines and so the behavior of magnetic braking roughly agrees with the above simple analysis.

To explore strong gravity regime, we consider an extreme relativistic star with $M/R = 0.44$, approaching the Buchdahl limit $M/R \rightarrow 4/9$. Recall that at the Buchdahl limit, the pressure at the center of the star ($r = 0$) becomes infinite, which causes the lapse function α vanish at the center. We therefore expect to see a very different evolution pattern of \bar{B} and $\hat{\Omega}$. Figure 10 shows the snapshots of \bar{B} and $\hat{\Omega}$ along the $\theta = 45^\circ$ line. We see that although the pattern of the curves is very different from the previous two cases, small-scale structures still develop at late times. The amplitude of the toroidal field is much larger and the oscillation timescale is much longer at small r than that at large r . It follows from Eqs. (130) and (131) that we can define the effective local Alfvén speed as

$$v_{\text{eff}}(r) = \sqrt{\frac{\alpha^3 \lambda^2}{\alpha R}} \left(\frac{B_0}{\sqrt{4\pi\rho}} \right) = \frac{\hat{\tau}}{\hat{t}} v_A. \quad (186)$$

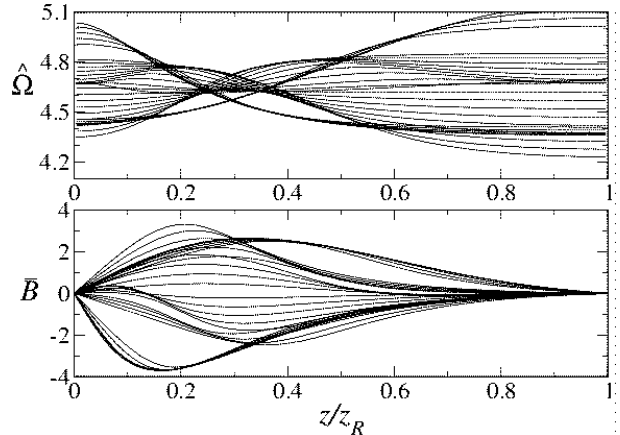


FIG. 11: Snapshots of \bar{B} (lower panel) and $\hat{\Omega}$ (upper panel) along the $\varpi/R = 0.5$ line for a relativistic star with $M/R = 0.44$. Analysis with FFT of the time series reveals that the initial data consists of mainly three modes with frequencies $\hat{f}_1 = 0.0356$, $\hat{f}_2 = 0.0622$ and $\hat{f}_3 = 0.0979$. Curves are plotted at time intervals $\Delta\hat{t} = 5$ from $\hat{t} = 0$ to $\hat{t} = 140$ (about 5 oscillation periods of the fundamental mode).

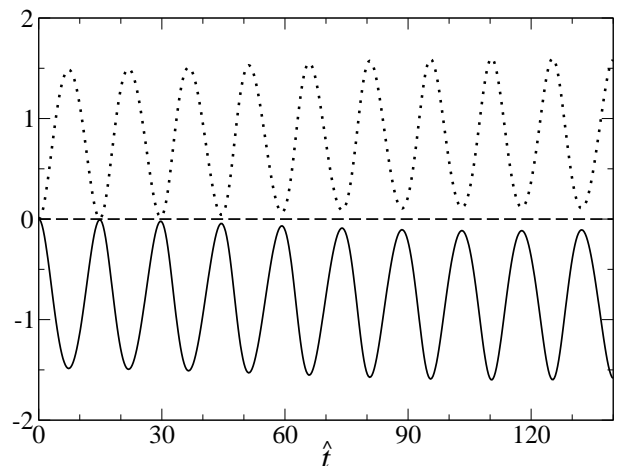


FIG. 12: Same as Fig. 6 but for a relativistic star with $M/R = 0.44$.

Hence the Alfvén speed is very small at the center when the Buchdahl limit is approached, which explains why the oscillation period is long close to the center.

Figure 11 shows the snapshots of \bar{B} and $\hat{\Omega}$ on the $\varpi/R = 0.5$ plane. For this extreme relativistic star, the solution of the MHD equations with the initial angular velocity distribution (172) is no longer close to the fundamental mode. We perform a fast Fourier transform

(FFT) on the time series $\bar{B}(\hat{t}; 0.5, \hat{u})$ for three different values of \hat{u} . We find that each of the three sets of time series consist mainly of three frequencies $\hat{f}_1 = 0.0356$, $\hat{f}_2 = 0.0622$ and $\hat{f}_3 = 0.0979$. We also see that the peak of the toroidal field shifts with increasing time to a lower value of z . This can be explained by the following physical argument. The initial angular velocity can be regarded as a superposition of waves of $B^{\hat{\phi}}$ traveling to $z = -z_R = -\sqrt{R^2 - \varpi^2}$ and $z = z_R$. The waves are reflected at the two points and travel backward. Since the value of r is smaller at smaller z , it follows from Eq. (186) that the local Alfvén speed decreases as z decreases. However, the equatorial symmetry condition on Ω forces the toroidal field to vanish at the equator. As a result, the waves pile up near the equator, causing the peak to shift to a smaller value of z .

From Eq. (180) we found $\hat{\Omega}_{\text{mean}} = 0.64$. Even though the $\hat{\Omega}$ in Fig. 11 consists of several modes, it still oscillates about this mean angular velocity. As in the previous cases, the rotational kinetic energy associated with the differential rotation transfers back and fro to the energy associated with the toroidal magnetic field (see Fig. 12).

2. $l = 2$ initial field (Cases IIa-IIc)

For the $l = 2$ field, we numerically integrate Eqs. (164) and (165) in the (\hat{u}, \hat{v}) coordinate system introduced in Section V B. The advantage of using these rather complicated coordinates is twofold. First, we only need to integrate a set of decoupled 1+1 evolution equations. Second, more importantly, small-scale structures will develop at late times in a direction across the poloidal field lines. Using other coordinate systems (e.g. standard Cartesian, spherical or cylindrical coordinates) will involve taking derivatives across the poloidal field lines, which will be numerically inaccurate when the finite-sized grid can no longer resolve the growth of small-scale structures. We will demonstrate this numerical inaccuracy in Section VI B. To estimate the numerical error of our code, we monitor the conserved integrals $\hat{e}_2(\hat{v})$ and $\hat{j}_2(\hat{v})$ defined in Eqs. (168) and (171) as well as second order convergence. We find that the fractional variation of \hat{e}_2 and \hat{j}_2 is less than 0.3% for all of our runs with our canonical grid allocation.

In the literature, the rotation law

$$u^t u_\phi = A^2 (\Omega_c - \Omega) \quad (187)$$

is often used to model differentially rotating relativistic stars (see, e.g. Ref. [62]). Here A is a constant. This law corresponds to, using the metric (89), the relation

$$\hat{\Omega} = \hat{\Omega}_p = \frac{1}{1 + \frac{\hat{r}^2 \sin^2 \theta}{\alpha^2 \hat{A}^2}}, \quad (188)$$

where $\hat{A} = A/R$ and we have ignored the frame dragging term for simplicity. In the Newtonian limit ($\alpha \rightarrow 1$), $\hat{\Omega}_p$

reduces to the so-called “ j -constant” law [63]. Unfortunately, this rotation law does not satisfy the constraint $B^j(0)\partial_j\Omega = 0$ at $r = R$. To “fix” this, we choose a modified rotation profile[71]

$$\hat{\Omega}(0; \hat{r}, \theta) = \hat{\Omega}_p(\hat{r}, \theta)f(\hat{r}) + \hat{\Omega}_b(\hat{r}, \theta)[1 - f(\hat{r})], \quad (189)$$

where $\hat{\Omega}_b$ is a function that satisfies the constraint at $r = R$ and f is a function which is close to 1 and drops rapidly to 0 at $\hat{r} = 1$. We also require $f'(1) = 0$. Specifically, we choose

$$f(\hat{r}) = \frac{f_F(\hat{r}) - f_F(1) + \frac{1}{2}f'_F(1)(1 - \hat{r}^2)}{f_F(0) - f_F(1) + \frac{1}{2}f'_F(1)} \quad (190)$$

$$f_F(\hat{r}) = \frac{1}{1 + \exp[(\hat{r} - b)/\epsilon]}, \quad (191)$$

where b and ϵ are constant parameters which we set to be $b = 0.8$ and $1/\epsilon = 25$. We set

$$\hat{\Omega}_b(\hat{r}, \theta) = \langle \hat{\Omega}_p(1, \theta) \rangle \hat{r}(2 - \hat{r}), \quad (192)$$

where

$$\begin{aligned} \langle \hat{\Omega}_p(1, \theta) \rangle &= \frac{1}{4\pi} \int_0^{2\pi} d\phi \int_0^\pi d\theta \sin \theta \hat{\Omega}_p(1, \theta) \quad (193) \\ &= \frac{\alpha_R^2 \hat{A}^2}{\sqrt{1 + \alpha_R^2 \hat{A}^2}} \tanh^{-1} \left(\frac{1}{\sqrt{1 + \alpha_R^2 \hat{A}^2}} \right) \quad (194) \end{aligned}$$

We set the parameter $\hat{A} = 1$ in all of our numerical calculations. The value of $\hat{\Omega}(0; r, \theta)$ chosen in this way is close to $\hat{\Omega}_p(r, \theta)$ except near the surface of the star, where the modification makes it satisfy the boundary condition $B^j(0)\partial_j\Omega = 0$ at $r = R$.

Figure 13 shows the evolution of the toroidal field and angular velocity along the line $\varpi/R = 0.5$ for a Newtonian star ($M/R \ll 1$). Magnetic braking causes the toroidal field and angular velocity to oscillate. We see that small-scale structures develop at late times, which is expected since the direction does not line up with any poloidal field line, while coherent oscillations are restricted to field lines.

Figure 15 shows the snapshots of \bar{B} and $\hat{\Omega}$ along the line $\hat{v} = 0.1$ (see Fig. 14) for the same star. Small-scale structures are not seen along this line since we are looking in the direction of a poloidal field line. We perform FFT on the time series of three chosen points on the line. We find that the FFT spectra consist of the same frequencies for the three points. The lowest four eigenfrequencies are determined to be 0.35, 0.65, 0.95 and 1.25 in our nondimensional units.

Similar to the $l = 1$ cases, we can define, from Eq. (171), a mean angular velocity at each \hat{v} by

$$\hat{\Omega}_{\text{mean}}(\hat{v}) = \hat{j}_2(\hat{v})/\hat{I}_2(\hat{v}), \quad (195)$$

where

$$\hat{I}_2(\hat{v}) = \int_0^1 d\hat{u} \frac{\sin^2 \theta}{\alpha^2 \lambda (3 \cos^2 \theta + 1)}. \quad (196)$$

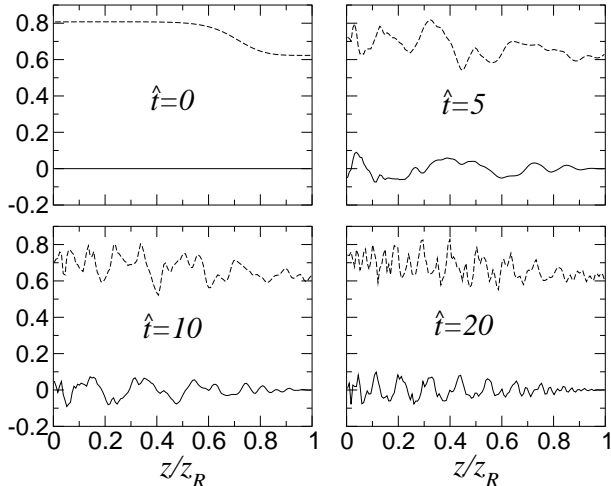


FIG. 13: Snapshots of \bar{B} (lower curves) and $\hat{\Omega}$ (upper curve) along the $\varpi/R = 0.5$ line for a Newtonian star ($M/R \ll 1$). The initial magnetic field is the $l = 2$ field given by Eq. (117). The surface of that star is located at $z = z_R = \sqrt{R^2 - \varpi^2}$. Since the direction does not line up with the field lines, the build-up of small-scale structure is observed, as expected.

For this Newtonian star, we found $\hat{\Omega}_{\text{mean}}(0.1) = 0.70$. We see from Fig. 15 that $\hat{\Omega}$ oscillates about this mean value. Figure 16 shows the evolution of the reduced energies at $\hat{v} = 0.1$. As expected, we see that both the reduced rotational kinetic energy \hat{e}_2^{rot} and magnetic energy \hat{e}_2^{mag} oscillate, while keeping the total energy \hat{e}_2 conserved.

Figure 17 shows the snapshots of \bar{B} and $\hat{\Omega}$ along the $\varpi/R = 0.5$ line for a relativistic star with $M/R = 0.3$. The graphs look qualitatively the same as the Newtonian situation. Similar to the $l = 1$ case, it is easy to see from Eqs. (164) and (165) that if the relativistic factors α and λ do not change significantly inside the star, the main relativistic effects are to cause time to dilate according to Eq. (185) and to increase the amplitude of the toroidal field by a factor of $1/\alpha$ for a given set of initial data. This explains the similarity of the features in Figs. 13 and 17, and that small-scale structures appear later for the relativistic star. Figure 18 shows the snapshots along the $\hat{v} = 0.1$ line, and Fig. 19 shows the evolution of the reduced energies. The angular velocity function $\hat{\Omega}(t; \hat{u}, 0.1)$ oscillates about the mean value $\hat{\Omega}_{\text{mean}}(0.1) = 0.45$. The FFT spectrum reveals the lowest four eigenfrequencies to be 0.14, 0.26, 0.38 and 0.62. Note that these frequencies are 40% of those of the Newtonian stars, which agrees with the time dilation effect predicted by Eq. (185). However, the ratio of the amplitudes of the toroidal field is much larger than the predicted value α . This is because the two stars do not have the same initial angular velocity profile [see Eqs. (188) and (189)].

Finally, we explore effect of strong gravity by consider-

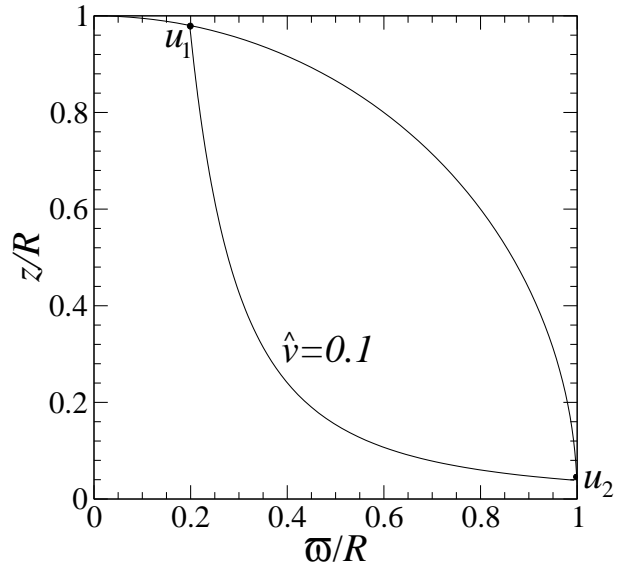


FIG. 14: The $\hat{v} = 0.1$ line.

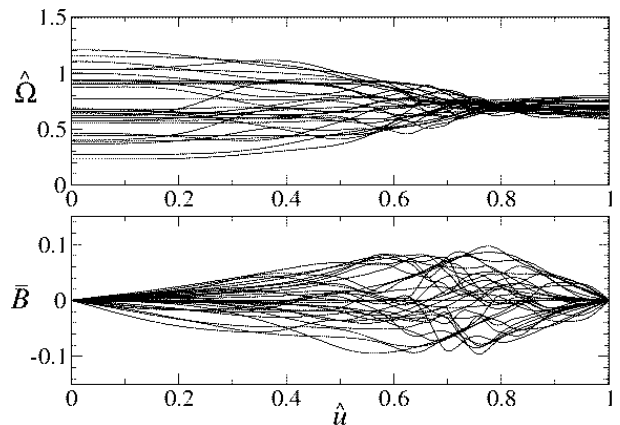


FIG. 15: Snapshots of \bar{B} (lower panel) and $\hat{\Omega}$ (upper panel) along the $\hat{v} = 0.1$ line for a Newtonian star ($M/R \ll 1$). The FFT spectrum indicates that the first four eigenfrequencies to be approximately 0.35, 0.65, 0.95 and 1.25. Curves are plotted at time intervals $\Delta \hat{t} = 0.5$ from $\hat{t} = 0$ to $\hat{t} = 15$ (about 5 oscillation periods of the fundamental mode).

ing a relativistic star with $M/R = 0.44$, approaching the Buchdahl limit. Figures 20 (21) shows the snapshots of \bar{B} and $\hat{\Omega}$ along the $\varpi/R = 0.5$ ($\hat{v} = 0.1$) line. Figure 22 shows the evolution of the reduced energies at $\hat{v} = 0.1$. We see that the behavior is qualitatively very different from the previous two stars. Small-scale structures still develop, but it happens at much later time. The oscil-

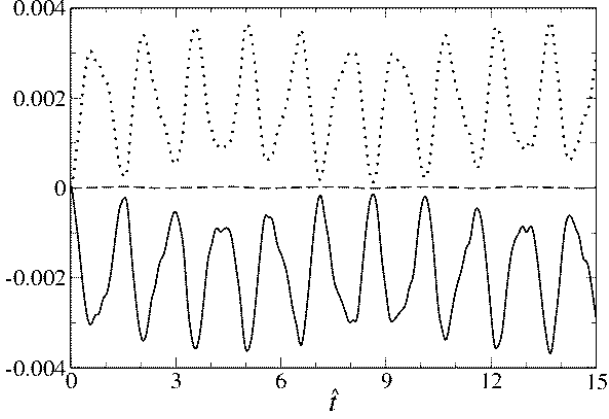


FIG. 16: Evolution of the reduced energies for a Newtonian star with $l = 2$ initial magnetic field. The solid line is $\hat{\epsilon}_2^{\text{rot}}(\hat{t}) - \hat{\epsilon}_2^{\text{rot}}(0)$, the dotted line is $\hat{\epsilon}_2^{\text{mag}}(\hat{t})$, and the dashed line is $\hat{\epsilon}_2 - \hat{\epsilon}_2^{\text{rot}}(0)$. All the reduced energies are evaluated at $\hat{v} = 0.1$.

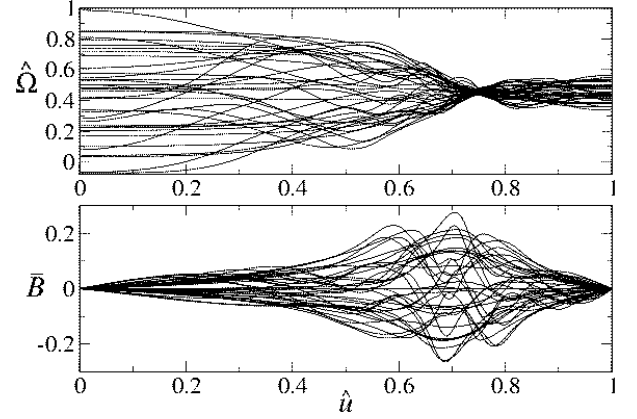


FIG. 18: Snapshots of \bar{B} (lower panel) and $\hat{\Omega}$ (upper panel) along the $\hat{v} = 0.1$ line for a relativistic star with $M/R = 0.3$. The FFT spectrum reveals that the first four eigenfrequencies to be 0.14, 0.26, 0.38 and 0.62. Curves are plotted at time intervals $\Delta\hat{t} = 1$ from $\hat{t} = 0$ to $\hat{t} = 35$ (about 5 oscillation periods of the fundamental mode).

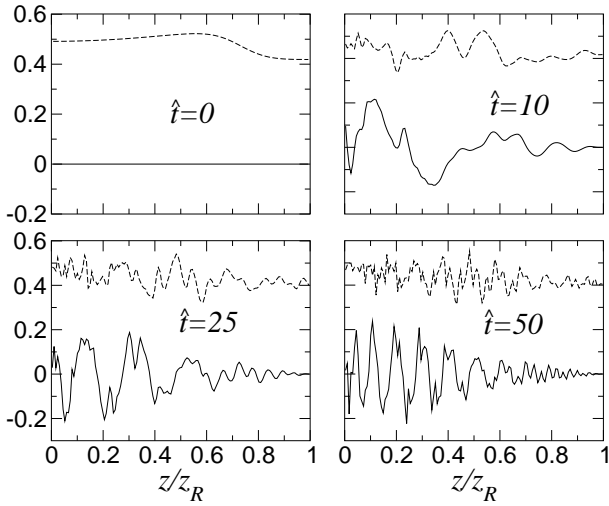


FIG. 17: Same as Fig. 13 but with $M/R = 0.3$.

lation amplitudes of \bar{B} and $\hat{\Omega}$ are much larger along the $\hat{v} = \text{constant}$ lines.

The growth of the toroidal field twists the poloidal field lines in the azimuthal direction. The magnetic field lines are therefore still confined to the surface spanned by the poloidal field lines. However, since we consider the situation in which the rotational timescale is much longer than the Alfvén timescale, the induced toroidal field is very small compared to the poloidal field. In order to see the small twist of the field lines, we multiply the toroidal field $B^{\hat{\phi}}$ by an arbitrary factor of $10v_A/\Omega_c R$ in Fig. 23,

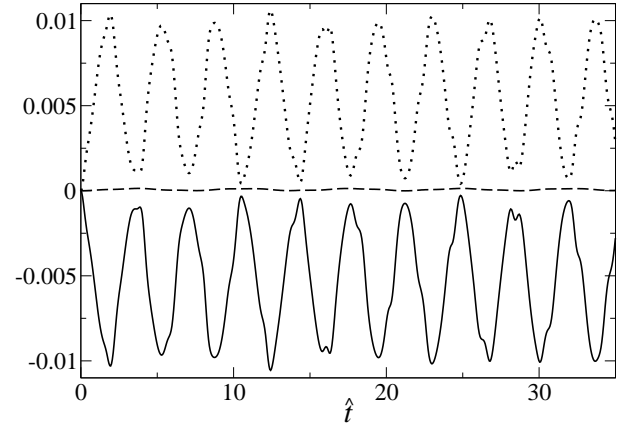


FIG. 19: Same as Fig. 16 but for a relativistic star with $M/R = 0.3$.

where the field lines on the $\hat{v} = 0.1$ surface is plotted for a relativistic star with $M/R = 0.3$. As expected, the oscillations of the toroidal field lines cause the total field lines to twist back and forth in the azimuthal direction. The field lines of relativistic stars with other compaction factors M/R behave in a similar way.

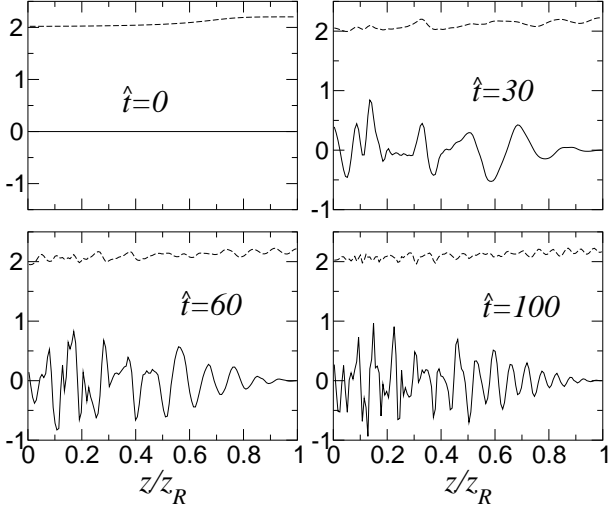


FIG. 20: Same as Fig. 13 but with $M/R = 0.44$ (The upper curve is $\hat{\Omega} + 2$).

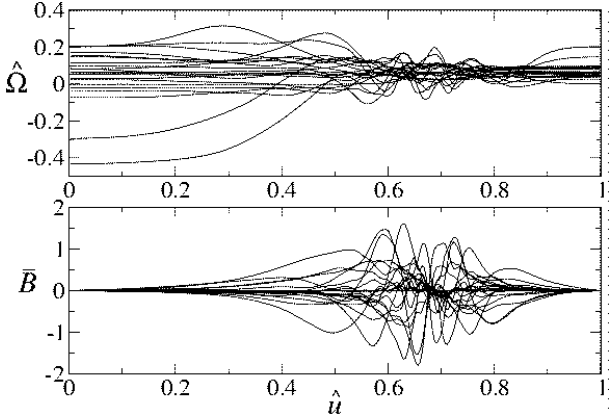


FIG. 21: Snapshots of \bar{B} (lower panel) and $\hat{\Omega}$ (upper panel) along the $\hat{v} = 0.1$ line for a relativistic star with $M/R = 0.44$. The FFT spectrum reveals that the first four eigenfrequencies to be 0.016, 0.031, 0.045 and 0.060. Curves are plotted at time intervals $\Delta\hat{t} = 15$ from $\hat{t} = 0$ to $\hat{t} = 300$ (about 5 oscillation periods of the fundamental mode).

B. Role of Viscosity (Case III)

Our previous results show that the phase mixing arising from magnetic braking is likely to induce irregular angular velocity flow. A significant meridional current will build up eventually, and thus may induce other magnetic instabilities and cause turbulence. Magnetic diffusion and viscosity will play a significant role on the subse-

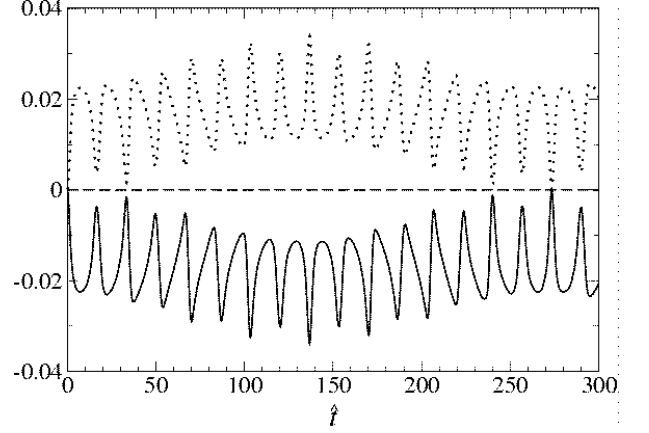


FIG. 22: Same as Fig. 16 but for a relativistic star with $M/R = 0.44$.

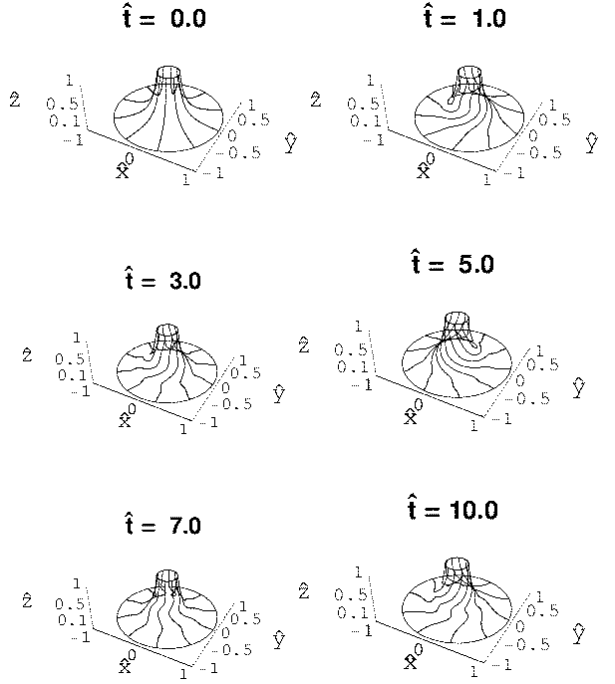


FIG. 23: The magnetic field lines as functions of time along the axisymmetric surface $\hat{v} = 0.1$ for a relativistic star with $M/R = 0.3$. The poloidal field lines are the same as the field lines at $\hat{t} = 0$. The toroidal field has been multiplied by an arbitrary factor of $10v_A/\Omega_c R$ so that they are more visible. The circles on the upper and lower ends are the boundary of the star, i.e., the lines of revolution generated by the points u_1 and u_2 in Fig. 14.

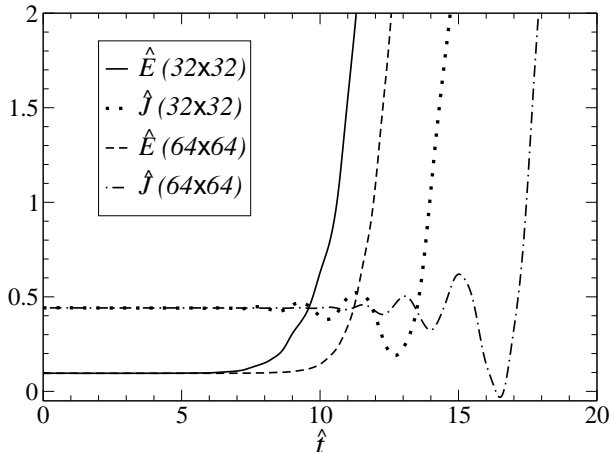


FIG. 24: Energy and angular momentum versus time by evolving Eqs. (146) and (147) for the $l = 2$ poloidal field using the cylindrical-like coordinates $(\hat{\varphi}, \hat{u})$ in the absence of viscosity. The compaction M/R is 0.3. The results for two resolutions 32×32 and 64×64 are plotted. The energy and angular momentum deviate from their initial values at late times because the finite-sized grid fails to resolve the small-scale structures built up by magnetic braking. Increasing the resolution postpones, but does not eliminate, the breakdown of conservation.

quent evolution. It has been shown in Newtonian MHD that magnetic diffusion will damp out the angular velocity oscillations along a poloidal line. The final state of the star will have a constant angular velocity profile on each magnetic surface (see [67] and references therein). Here we wish to discuss the role of viscosity in damping differential motion. Microscopic viscosity in a typical neutron star is very small, and its timescale is very long compared to the rotational period [64]. Here we may regard viscosity as a “turbulent viscosity,” which models the effects of turbulence via an effective shear viscosity. The typical turbulent viscosity is $\nu \sim l\Delta v$ (see Ref. [55], § 33), where l is the length scale of the largest turbulent eddies and Δv is the velocity fluctuation over the distance l . This turbulent viscosity is much larger than the microscopic viscosity, and can affect the flow on a dynamical timescale.

We solve the MHD equations (164) and (165) with viscosity $\hat{\nu} \neq 0$. We only present one case here, as the result is qualitatively similar for all the other cases. The initial poloidal field is given by the $l = 2$ field and the M/R of the star is 0.3. The viscosity coefficient $\hat{\nu}$ is set to be 0.002. This value is chosen so that the toroidal field and angular velocity can go through several Alfvén oscillations before the viscosity damps the oscillations.

As mentioned in Section VB, the $(\hat{u}, \hat{\nu})$ coordinates are not convenient when viscosity is present. We use the cylindrical-like coordinates $(\hat{\varphi}, \hat{u})$ introduced in Sec-

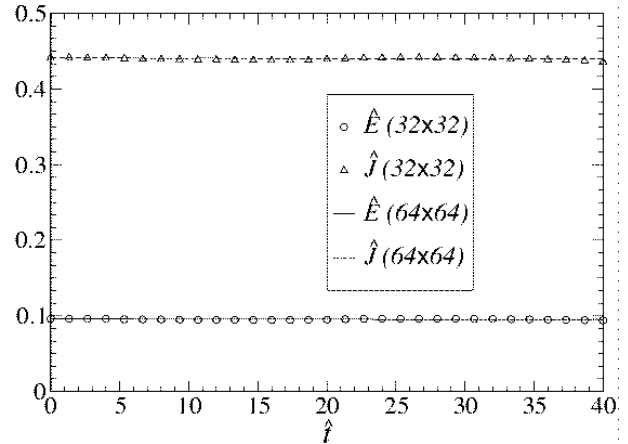


FIG. 25: Same as Fig. 24 but with viscosity $\hat{\nu} = 0.002$. Viscosity suppresses the formation of small-scale structures. Hence the integrals can be conserved accurately even in cylindrical coordinates.

tion VA in this case. In the absence of viscosity, we are not able to integrate the MHD equations accurately in these coordinates very long because our finite-sized grid can no longer resolve the small-scale structures that develop at late times. Figure 24 illustrates the resulting numerical inaccuracy by plotting the energy \hat{E} and angular momentum \hat{J} computed from the numerical data as a function of time. We evolve the MHD equations with resolutions 32×32 and 64×64 . We see that the two conserved integrals deviate from their initial values at late times. Doubling the resolution does not eliminate, but only postpones, the breakdown of \hat{E} and \hat{J} conservation. Hence in the absence of viscosity, we must use the $(\hat{u}, \hat{\nu})$ coordinates to ensure a stable evolution. However, when we include a small viscosity $\hat{\nu} = 0.002$, the situation changes drastically. The viscosity suppresses the build up of small-scale structure. As a result, the numerical inaccuracy disappears (see Fig. 25). The fluctuation of energy \hat{E} is 3% (0.4%) in 32×32 (64×64) resolution. The fluctuation of angular momentum \hat{J} is 1% (0.4%) in 32×32 (64×64) resolution.

Figure 26 shows the snapshots of \hat{B} and $\hat{\Omega}$ at the equator. We see that the star is driven to uniform rotation with no toroidal field at late times, as expected. Since angular momentum is conserved, we can calculate the final angular velocity from Eq. (153), which is also valid for the $l = 2$ field. We obtain

$$\hat{\Omega}_{\text{final}} = \hat{J}/\hat{I}, \quad (197)$$

$$\hat{I} = 3\alpha_R \int_0^1 d\varpi \varpi^3 \sqrt{1 - \varpi^2} \int_0^1 \frac{d\hat{u}}{\alpha^2 \lambda}. \quad (198)$$

Not surprisingly, our numerical value of $\hat{\Omega}_{\text{final}}$ shown in Fig. 26 agrees with the above formula, $\hat{\Omega}_{\text{final}} = 0.425$.

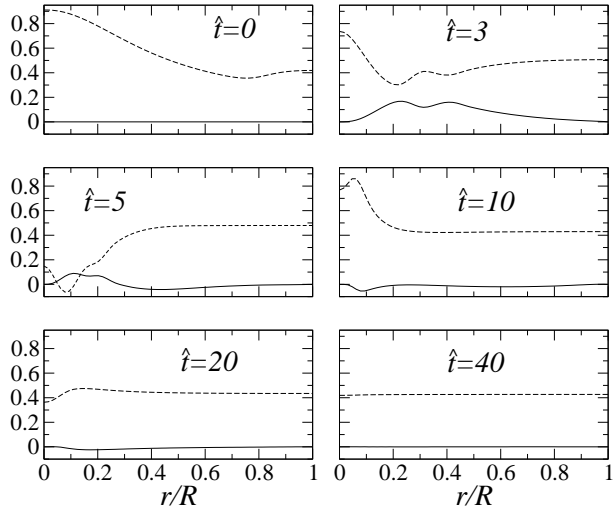


FIG. 26: Snapshots of \hat{B} (solid lines) and $\hat{\Omega}$ (dashed lines) at the equator in the presence of viscosity. The coefficient of viscosity is set to be $\hat{\nu} = 0.002$. The toroidal field vanishes and the star becomes rigidly rotating at late times, as expected.

Finally, Fig. 27 shows the evolution of $\hat{E}_{\text{rot}}(\hat{t})$, $\hat{E}_{\text{mag}}(\hat{t})$, and $\hat{E}_{\text{vis}}(\hat{t})$. We see that a portion of rotational energy transfers to magnetic energy of the toroidal field. Both energies are eventually turned into heat. The total energy is conserved up to the truncation error, which decreases with increasing resolution.

VII. SUMMARY AND DISCUSSION

We have studied the magnetic braking in differentially rotating, relativistic stars. The results we found are very different from the models studied in Papers I and II. The models in Paper I are incompressible and one-dimensional (infinite cylinders), the models in Paper II are compressible and one-dimensional (infinite cylinders), while the models in this paper are incompressible and two-dimensional (axisymmetric, finite stars). In Papers I and II, the Newtonian MHD equations were evolved while here we evolved the relativistic MHD equations with the assumption that the initial poloidal fields is large compared to rotational energy, but weak compared to the gravitational binding energy. In Papers I and II, it was found that magnetic braking generates coherent toroidal magnetic fields and laminar velocity flows. In the models considered here, we found that the field breaks down because of the phase mixing both in Newtonian and relativistic regimes. Our analysis indicates that the phase mixing is a result of the geometry of the stars and the poloidal field lines: phase mixing is absent in the infinite cylinders of Papers I and II simply because the systems

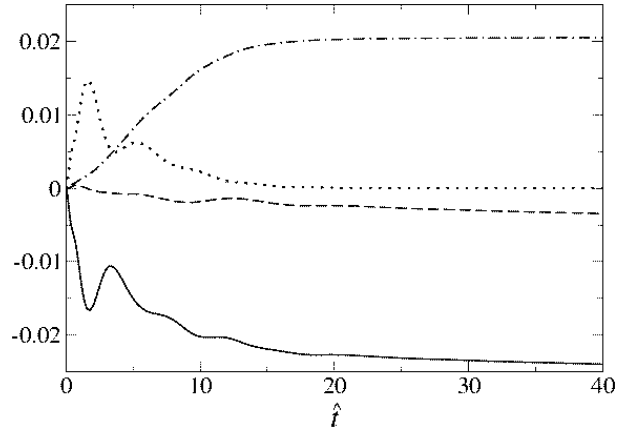


FIG. 27: Evolution of energies for a relativistic star with $M/R = 0.3$ in the presence of viscosity. The solid line is $\hat{E}_{\text{rot}}(\hat{t}) - \hat{E}_{\text{rot}}(0)$, the dotted line is $\hat{E}_{\text{mag}}(\hat{t})$, the dot-dashed line is $\hat{E}_{\text{vis}}(\hat{t})$, and the dashed line is the sum of the three lines, i.e. $\hat{E}_{\text{rot}}(\hat{t}) + \hat{E}_{\text{mag}}(\hat{t}) + \hat{E}_{\text{vis}}(\hat{t}) - \hat{E}_{\text{rot}}(0)$, which should remain constant and equal to 0. The deviation from zero of the dashed curve is due to truncation error of our code, which decreases with increasing resolution.

are highly symmetric. However, even in finite stars, if viscosity is sufficiently strong, the toroidal fields may be damped before phase mixing becomes appreciable.

Differential rotation is damped by the presence of poloidal magnetic fields and viscosity. Magnetic braking causes the toroidal fields and angular velocities to undergo oscillations along each poloidal field line. In the regime explored in this paper, the oscillations along a given field line are independent of those along other lines. This phase mixing effect is likely to stir up turbulent-like motion. When viscosity is present, the star ultimately is driven toward uniform rotation. When the compactness of the star, M/R , is not very large, the effect of magnetic braking in a relativistic star is similar to the Newtonian case, but the timescale of the braking process is increased roughly by a factor $(1 - 2M/R)^2$. When M/R approaches the Buchdahl limit $4/9$, the braking process is strongly affected by the spacetime curvature. Strong toroidal fields pile up at small r along each field line, since the proper time elapses more slowly than at larger r for the same amount of coordinate time. The whole process of magnetic braking can take much longer in this case than in the Newtonian situation.

The assumptions necessary to bring the 2+1 MHD equations into a set of 1+1 equations are that the system is axisymmetric; viscosity, magnetic diffusion and meridional currents can be neglected; and both magnetic and rotational energies are much smaller than the gravitational binding energy. The condition $E_{\text{mag}} \gg E_{\text{rot}}$ is a sufficient but may not be a necessary condition for the meridional currents to remain small in tens of Alfvén

times. It is possible that the meridional currents can still be small compared to the rotational velocity even if this condition is not satisfied. If this is the case, our analysis here will still be valid. It is possible that most young neutron stars or merged binary neutron star remnants do not have strong poloidal fields and the opposite limit $E_{\text{rot}} \gg E_{\text{mag}}$ may be more relevant. More detailed MHD calculations are required to study the general case.

The microscopic viscous timescale is of order $t_\nu = R^2/8\nu \approx 10^9$ s for a typical neutron star, where $\nu = 347\rho^{9/4}T^{-2}$ cm² s⁻¹ and T is temperature [64]. However, turbulent viscosity can be much bigger and might drive the star toward uniform rotation on much shorter timescale. The Alfvén timescale in a neutron star with magnetic field $B = 10^{12}$ G is tens of seconds (Paper I). Hence, the effect of magnetic field is much more important than microscopic viscosity in neutron stars. Magnetic braking may have important consequences for gravitational wave signals and gamma-ray bursts, as discussed in the Introduction.

A significant amount of meridional current may also be generated as a result of the phase mixing. Our calculations do not take into account the later build-up of meridional currents, which may induce convective instabilities [65], driving the seed magnetic field to high values greatly exceeding 10^{12} G [66]. The meridional currents may also induce other possible MHD instabilities, which may contribute to the redistribution of angular momentum [53, 67]. Our goal here is to show that even in the simplest case, magnetic braking can also induce irregular, turbulent-like behavior.

More realistic evolutionary calculations of magnetic braking in neutron stars should clarify some of the above issues. One computational subtlety is that the Alfvén timescale is usually much longer than the dynamical timescale of the star. In this regime it may prove too taxing to a relativistic MHD code to evolve a differentially rotating star for the required length of time for magnetic braking to take effect. One possibility is to treat part of the evolution in the quasistatic approximation, as in a typical stellar evolution code, up to the moment that stable equilibrium can no longer be sustained. One other possibility is to artificially amplify the magnetic field so that the effect of magnetic braking will show up in a computationally manageable timescale, and then scale the results for smaller ratios. Still another approach is to use implicit differencing scheme to avoid the Courant constraint on the evolution timestep. However, our calculations suggest that small-scale irregular angular velocity flows and meridional currents are likely to grow during the process of magnetic braking. The ability of a numerical code (finite difference or spectral) to resolve this behavior on ever decreasing scales is an important challenge that will require further analysis. We hope to tackle the more general problems in the near future by means of numerical simulations in full general relativity.

We thank Charles Gammie and Jon McKinney for useful discussions. This work was supported in part by

NSF Grants PHY-0090310 and PHY-0205155 and NASA Grant NAG 5-10781 at UIUC.

APPENDIX A: VALIDITY OF IGNORING v^r AND v^θ

The main effect of magnetic braking is to wind up the frozen-in magnetic field and generate toroidal fields, which back-react on the angular velocity, $v^\phi = \Omega$. The change in angular velocity ultimately drives a meridional current. In this appendix, we estimate the timescale for $v^{\hat{r}}$ and $v^{\hat{\theta}}$ to become comparable to $v^{\hat{\phi}}$. Here we only study the simplest case: a differentially rotating, incompressible Newtonian star, with an initial $l = 1$ poloidal field $\mathbf{B}(0) = B_0 \mathbf{e}_z$, and zero viscosity.

We start from the Newtonian MHD equations (1)–(4). We neglect viscosity in this appendix. We find it convenient to work in cylindrical coordinates (ϖ, ϕ, z) . The meridional components of the velocity are $v^\varpi = \sin\theta v^{\hat{r}} + \cos\theta v^{\hat{\theta}}$, and $v^z = \cos\theta v^{\hat{r}} - \sin\theta v^{\hat{\theta}}$. The MHD equations become

$$\partial_t B^\phi = B_0 \partial_z \Omega + [(B^z - B_0) \partial_z \Omega + B^\varpi \partial_\varpi \Omega - v^j \partial_j B^\phi], \quad (\text{A1})$$

$$\partial_t \Omega = \frac{B_0}{4\pi\rho} \partial_z B^\phi + \left[\frac{1}{4\pi\rho} \left(B^\varpi \partial_\varpi B^\phi + \frac{2}{\varpi} B^\varpi B^\phi \right) - v^j \partial_j \Omega - \frac{2}{\varpi} v^\varpi \Omega \right], \quad (\text{A2})$$

$$\partial_t B^i = B^j \partial_j v^i - v^j \partial_j B^i, \quad (\text{A3})$$

$$\partial_t v^\varpi = -v^j \partial_j v^\varpi + \varpi \Omega^2 - \frac{1}{\rho} \partial_\varpi P - \partial_\varpi \Phi - \frac{1}{8\pi\rho} \partial_\varpi B^2 + \frac{1}{4\pi\rho} [B^j \partial_j B^\varpi - \varpi (B^\phi)^2] \quad (\text{A4})$$

$$\partial_t v^z = -v^j \partial_j v^z - \frac{1}{\rho} \partial_z P - \partial_z \Phi - \frac{1}{8\pi\rho} \partial_z B^2 + \frac{1}{4\pi\rho} B^j \partial_j B^z, \quad (\text{A5})$$

$$\partial_t B^\varpi = v^j \partial_j B^\varpi - B^j \partial_j v^\varpi, \quad (\text{A6})$$

$$\partial_t B^z = v^j \partial_j B^z - B^j \partial_j v^z, \quad (\text{A7})$$

where i and j denotes ϖ and z , and the summation convention is assumed. At $t = 0$, we assume $v^\varpi(0; \varpi, z) = v^z(0; \varpi, z) = 0$, $v^\phi(0; \varpi, z) = \Omega(0; \varpi, z)$, $\mathbf{B}(0; \varpi, z) = B_0 \mathbf{e}_z$, and the star is in hydrostatic equilibrium:

$$\varpi \Omega^2(0; \varpi, z) - \frac{1}{\rho} \partial_\varpi P(0; \varpi, z) - \partial_\varpi \Phi(0; \varpi, z) = 0, \quad (\text{A8})$$

$$-\frac{1}{\rho} \partial_z P(0; \varpi, z) - \partial_z \Phi(0; \varpi, z) = 0, \quad (\text{A9})$$

where we have used Eqs. (A4) and (A5). After grouping these equilibrium terms, we see that the only remaining nonvanishing term at $t = 0$ in Eqs. (A1)–(A7) is $B_0 \partial_z \Omega$, the first term on the right side of Eq. (A1). This simply tells us the obvious fact that when there is differential

rotation along the initial field lines (which is in the z -direction for this initial field), a toroidal field B^ϕ will be generated by a term linear in Ω . It follows from Eq. (A2) that the toroidal field will then modify Ω . Given our assumptions of slow rotation and weak magnetic field, all the other terms are of higher order, at least at small t . This is the reason we neglect them in this paper. However, it is possible that v^ϖ and v^z will become important at late times.

Here we crudely estimate the timescale in which v^ϖ and v^z are driven to a magnitude comparable to v^ϕ by the change of Ω induced by magnetic braking. We focus on Eq. (A4). We assume that the pressure P and gravitational potential Φ in our nearly spherical configuration do not change and set $v^\varpi = v^z = 0$, $B^\varpi = 0$, and $B^z = B_0$ on the right side of Eq. (A4). Using Eq. (A8), Eq. (A4) becomes

$$\partial_t v^\varpi = \varpi[\Omega^2(t) - \Omega^2(0)] - \frac{[B^\phi(t)]^2}{4\pi\rho\varpi}. \quad (\text{A10})$$

We then substitute for Ω and B^ϕ the analytic solutions given by Eqs. (55) and (56). For simplicity, we assume that only one mode is present, and write

$$\Omega(t) = \Omega(0) + \epsilon \left(1 - \frac{\varpi^2}{R^2}\right) \cos k_n z (1 - \cos \omega_n t), \quad (\text{A11})$$

$$B_1^\phi(t) = B_0 \left(\frac{\varpi\epsilon}{v_A}\right) \left(1 - \frac{\varpi^2}{R^2}\right) \sin k_n z \sin \omega_n t, \quad (\text{A12})$$

where ϵ is a constant parameter of dimension 1/time, measuring the degree of differential rotation along the initial magnetic field lines. We assume that the star may have a high degree of differential rotation so that ϵ can be of the same order as $\Omega(0)$. The factor $(1 - \varpi^2/R^2)$ is inserted to make both Ω and B^ϕ regular at $\varpi = R$. Equation (A10) can now be solved analytically. The growth of v^ϖ is dominated by the terms that go linearly in time:

$$v^\varpi \approx t\varpi\epsilon^2 \left(1 - \frac{\varpi^2}{R^2}\right) \left[\frac{2\Omega(0)}{\epsilon} \cos k_n z + 2 \left(1 - \frac{\varpi^2}{R^2}\right) \cos^2 k_n z - \frac{1}{2} \left(1 - \frac{\varpi^2}{R^2}\right) \right]. \quad (\text{A13})$$

Hence v^ϖ will be comparable to $v^\phi \sim \Omega(0)\varpi$ when $t \gtrsim t_c \sim \Omega(0)/\epsilon^2 > 1/\Omega(0)$. Hence $t_c \gtrsim P_{\text{rot}}$, where P_{rot} is a rotation period. It follows from the incompressibility condition $\nabla \cdot \mathbf{v} = 0$ that v^z is in general of the same order as v^ϖ . Therefore, v^z will also develop on the timescale t_c . On the other hand, the timescale for magnetic braking to affect v^ϕ and generate B^ϕ is t_A , the Alfvén timescale. Although our calculation is done on a Newtonian model with an $l = 1$ initial field, we expect that the result is similar in general relativity and with other initial magnetic field configurations.

Our estimate is based on dropping all the terms on the right side of Eq. (A4) which are of higher order at early

time. This crude calculation therefore does not take into account the possibility of the growth of other instabilities, like the magnetorotational instability (MRI). However, the growth time of this instability is also of order P_{rot} (see e.g., Ref. [53], Section IV). Hence we conclude that our numerical results are valid as long as the Alfvén timescale $t_A \ll P_{\text{rot}}$, or equivalently $E_{\text{rot}} \ll E_{\text{mag}}$.

Although our analysis in this paper is restricted to the early phases of the evolution $P_{\text{rot}} \gg t \gtrsim t_A$ in the slow rotation, weak magnetic field limit, we are able to determine the nonlinear evolution of the angular velocity and toroidal magnetic field profiles during this period for a fully relativistic, differentially rotating star.

APPENDIX B: TRANSFORMATION BETWEEN \hat{u} , \hat{v} , r AND θ FOR $l = 2$ FIELD

To solve Eqs. (164) and (165), we need to know the transformation between r , θ and \hat{u} , \hat{v} . In this appendix, we show the required transformation.

It is convenient to introduce the cylindrical variables

$$\hat{\omega} = \hat{r} \sin \theta, \quad \hat{z} = \hat{r} \cos \theta, \quad (\text{B1})$$

where $\hat{r} = r/R$. We also define an auxiliary variable

$$\hat{u}_* = u/R^2 = -\hat{r}^2(3 \cos^2 \theta - 1). \quad (\text{B2})$$

The relations between $\hat{\omega}$, \hat{z} , and \hat{u}_* , \hat{v} are

$$\hat{u}_* = \hat{\omega}^2 - 2\hat{z}^2, \quad (\text{B3})$$

$$\hat{v} = \frac{3\sqrt{3}}{2} \hat{\omega}^2 \hat{z}. \quad (\text{B4})$$

For a given value of \hat{v} , we denote by $\hat{\omega}_1$ and $\hat{\omega}_2$ (with $\hat{\omega}_2 > \hat{\omega}_1$) the two points at which the $\hat{v} = \text{constant}$ line intercepts the surface of the star $\hat{r} = 1$. Substituting $\hat{z} = \sqrt{1 - \hat{\omega}^2}$ in Eq. (B4), we obtain the equation for $\hat{\omega}_1$ and $\hat{\omega}_2$:

$$\hat{v} = \frac{3\sqrt{3}}{2} \hat{\omega}^2 \sqrt{1 - \hat{\omega}^2}. \quad (\text{B5})$$

The equation can be turned into a cubic equation and the solution is given by

$$\hat{\omega}_1 = \sqrt{\frac{1}{3} \left[1 + 2 \cos \left(\psi + \frac{4}{3}\pi \right) \right]}, \quad (\text{B6})$$

$$\hat{\omega}_2 = \sqrt{\frac{1}{3} (1 + 2 \cos \psi)}, \quad (\text{B7})$$

$$\psi = \frac{2}{3} \sin^{-1} \hat{v}. \quad (\text{B8})$$

It follows from Eqs. (B3) and (B4) that the corresponding \hat{u}_{1*} and \hat{u}_{2*} are given by

$$\hat{u}_{j*} = \hat{\omega}_j^2 - \frac{8\hat{v}^2}{27\hat{\omega}_j^4}, \quad (j = 1, 2). \quad (\text{B9})$$

The transformation from (r, θ) to (\hat{u}, \hat{v}) can be performed by the following procedure. We first compute \hat{u}_* and \hat{v} from Eqs. (B1)–(B4). We then compute \hat{u}_{1*} and \hat{u}_{2*} from Eqs. (B6)–(B9). Finally, we compute \hat{u} by the formula [see Eq. (162)]

$$\hat{u} = \frac{\hat{u}_* - \hat{u}_{1*}}{\hat{u}_{2*} - \hat{u}_{1*}}. \quad (\text{B10})$$

To transform from (\hat{u}, \hat{v}) to (r, θ) , we first compute \hat{u}_{1*} and \hat{u}_{2*} from Eqs. (B6)–(B9). Next we calculate \hat{u}_* from Eq. (B10). We then solve Eqs. (B3) and (B4) to obtain $\hat{\omega}$ and \hat{z} . The two equations can be combined into a cubic equation, which is solved by the standard cubic equation formula. Finally, the values of r and θ is obtained from Eq. (B1).

APPENDIX C: FINITE DIFFERENCING SCHEME

In this appendix, we describe in details our finite differencing scheme for the $l = 1$ MHD equations (151) and (152) in the presence of viscosity. The other cases are treated in a similar fashion.

We define

$$X_{i,j}^n = X(\hat{t}^n; \hat{u}_i, \hat{\omega}_j), \quad (\text{C1})$$

where X is any variables and

$$\hat{t}^n = n\Delta\hat{t}, \quad \hat{u}_i = i\Delta\hat{u}, \quad \hat{\omega}_j = j\Delta\hat{\omega}. \quad (\text{C2})$$

We use a uniform spatial grid ($\Delta\hat{u} = \text{constant}$, $\Delta\hat{\omega} = \text{constant}$) and a uniform time step ($\Delta\hat{t} = \text{constant}$) in our calculations. We store \hat{B} at grid points (i, j) and $\hat{\Omega}$ at $(i + 1/2, j)$. We compute the right side of Eqs. (151) and (152) by the following finite difference approximation:

$$\partial_{\hat{t}}\hat{B}(t^n; \hat{u}_i, \hat{\omega}_j) \approx f_{B;i,j}(\hat{\Omega}^n), \quad (\text{C3})$$

$$\begin{aligned} \partial_{\hat{t}}\hat{\Omega}(t^n; \hat{u}_{i+1/2}, \hat{\omega}_j) &\approx f_{\Omega;i+1/2,j}(\hat{B}^n) \\ &+ f_{v;i+1/2,j}(\hat{\Omega}^n), \end{aligned} \quad (\text{C4})$$

where

$$f_{B;i,j}(\hat{\Omega}^n) = \frac{\alpha_{i,j}\lambda_{i,j}}{\sqrt{1-\hat{\omega}_j^2}} \left(\frac{\hat{\Omega}_{i+1/2,j}^n - \hat{\Omega}_{i-1/2,j}^n}{\Delta\hat{u}} \right) \quad (\text{C5})$$

$$f_{\Omega;i+1/2,j}(\hat{B}^n) = \frac{\alpha_{i+1/2,j}^2\lambda_{i+1/2,j}}{\alpha_R\sqrt{1-\hat{\omega}_j^2}} \left(\frac{\hat{B}_{i+1,j}^n - \hat{B}_{i,j}^n}{\Delta\hat{u}} \right) \quad (\text{C6})$$

We use the expression in Eq. (149) to compute the finite difference term, $f_{v;i+1/2,j}(\hat{\Omega}^n)$, for $[\partial_{\hat{t}}\hat{\Omega}(t^n; \hat{u}_{i+1/2}, \hat{\omega}_j)]_{\text{vis}}$. Specifically, we first calculate $\partial_{\hat{u}}\hat{\Omega}$, $\partial_{\hat{u}}^2\hat{\Omega}$, $\partial_{\hat{\omega}}\hat{\Omega}$, $\partial_{\hat{\omega}}^2\hat{\Omega}$ and $\partial_{\hat{\omega}}\partial_{\hat{u}}\hat{\Omega}$ by standard central differencing, and then compute $\partial_{\hat{r}}\hat{\Omega}$, $\partial_{\hat{r}}^2\hat{\Omega}$, $\partial_{\hat{\theta}}\hat{\Omega}$ and $\partial_{\hat{\theta}}^2\hat{\Omega}$ by the transformation formulae

$$\partial_{\hat{r}}\hat{\Omega} = \frac{\hat{\omega}}{\hat{r}}\partial_{\hat{\omega}}\hat{\Omega} + \frac{\hat{u}}{\hat{r}(1-\hat{\omega}^2)}\partial_{\hat{u}}\hat{\Omega} \quad (\text{C7})$$

$$\partial_{\hat{\theta}}\hat{\Omega} = \hat{u}\sqrt{1-\hat{\omega}^2}\partial_{\hat{\omega}}\hat{\Omega} - \frac{\hat{\omega}}{\sqrt{1-\hat{\omega}^2}}(1-\hat{u}^2)\partial_{\hat{u}}\hat{\Omega} \quad (\text{C8})$$

$$\begin{aligned} \partial_{\hat{r}}^2\hat{\Omega} &= \frac{\hat{\omega}^2}{\hat{r}^2}\partial_{\hat{\omega}}^2\hat{\Omega} + \frac{\hat{u}^2}{\hat{r}^2(1-\hat{\omega}^2)^2}\partial_{\hat{u}}^2\hat{\Omega} + \frac{2\hat{\omega}\hat{u}}{\hat{r}^2(1-\hat{\omega}^2)}\partial_{\hat{\omega}}\partial_{\hat{u}}\hat{\Omega} \\ &+ \frac{3\hat{\omega}^2\hat{u}}{\hat{r}^2(1-\hat{\omega}^2)^2}\partial_{\hat{u}}\hat{\Omega} \end{aligned} \quad (\text{C9})$$

$$\begin{aligned} \partial_{\hat{\theta}}^2\hat{\Omega} &= \hat{u}^2(1-\hat{\omega}^2)^2\partial_{\hat{\omega}}^2\hat{\Omega} + \frac{\hat{\omega}^2}{1-\hat{\omega}^2}(1-\hat{u}^2)^2\partial_{\hat{u}}^2\hat{\Omega} \\ &- 2\hat{\omega}\hat{u}(1-\hat{u}^2)\partial_{\hat{\omega}}\partial_{\hat{u}}\hat{\Omega} - \hat{\omega}\partial_{\hat{\omega}}\hat{\Omega} \\ &- \hat{u}(1-\hat{u}^2)\frac{1+2\hat{\omega}^2}{1-\hat{\omega}^2}\partial_{\hat{u}}\hat{\Omega}. \end{aligned} \quad (\text{C10})$$

Finally, we compute $f_{v;i+1/2,j}(\hat{\Omega}^n)$ using Eq. (149).

We use an iterated Crank-Nicholson [57] scheme to evolve Eqs. (C3) and (C4). To be specific, we first predict \hat{B} and $\hat{\Omega}$ at the next time step by

$${}^{(1)}\hat{B}_{i,j}^{n+1} = \hat{B}_{i,j}^n + \Delta t f_{B;i,j}(\hat{\Omega}^n), \quad (\text{C11})$$

$$\begin{aligned} {}^{(1)}\hat{\Omega}_{i+1/2,j}^{n+1} &= \hat{\Omega}_{i+1/2,j}^n + \Delta t [f_{B;i+1/2,j}(\hat{B}^n) \\ &+ f_{v;i+1/2,j}(\hat{\Omega}^n)]. \end{aligned} \quad (\text{C12})$$

Next we estimate \hat{B} and $\hat{\Omega}$ at the next half time step by

$${}^{(1)}\hat{B}_{i,j}^{n+1/2} = \frac{1}{2} [\hat{B}_{i,j}^n + {}^{(1)}\hat{B}_{i,j}^{n+1}], \quad (\text{C13})$$

$${}^{(1)}\hat{\Omega}_{i+1/2,j}^{n+1/2} = \frac{1}{2} [\hat{\Omega}_{i+1/2,j}^n + {}^{(1)}\hat{\Omega}_{i+1/2,j}^{n+1}]. \quad (\text{C14})$$

We then use these variables to obtain a more accurate estimate of \hat{B} and $\hat{\Omega}$ at the next time step:

$${}^{(2)}\hat{B}_{i,j}^{n+1} = \hat{B}_{i,j}^n + \Delta t f_{B;i,j}({}^{(1)}\hat{\Omega}^{n+1/2}), \quad (\text{C15})$$

$$\begin{aligned} {}^{(2)}\hat{\Omega}_{i+1/2,j}^{n+1} &= \hat{\Omega}_{i+1/2,j}^n + \Delta t [f_{B;i+1/2,j}({}^{(1)}\hat{B}^{n+1/2}) + \\ &f_{v;i+1/2,j}({}^{(1)}\hat{\Omega}^{n+1/2})]. \end{aligned} \quad (\text{C16})$$

To ensure the stability of this finite differencing scheme, we have to do this ‘‘corrector’’ step one more time [57]. Hence we compute

$${}^{(2)}\hat{B}_{i,j}^{n+1/2} = \frac{1}{2} [\hat{B}_{i,j}^n + {}^{(2)}\hat{B}_{i,j}^{n+1}], \quad (\text{C17})$$

$${}^{(2)}\hat{\Omega}_{i+1/2,j}^{n+1/2} = \frac{1}{2} [\hat{\Omega}_{i+1/2,j}^n + {}^{(2)}\hat{\Omega}_{i+1/2,j}^{n+1}], \quad (\text{C18})$$

and use them to obtain the final values of \hat{B} and $\hat{\Omega}$ at the next time step:

$$\hat{B}_{i,j}^{n+1} = \hat{B}_{i,j}^n + \Delta t f_{B;i,j}({}^{(2)}\hat{\Omega}^{n+1/2}), \quad (\text{C19})$$

$$\begin{aligned} \hat{\Omega}_{i+1/2,j}^{n+1} &= \hat{\Omega}_{i+1/2,j}^n + \Delta t [f_{B;i+1/2,j}({}^{(2)}\hat{B}^{n+1/2}) \\ &+ f_{v;i+1/2,j}({}^{(2)}\hat{\Omega}^{n+1/2})]. \end{aligned} \quad (\text{C20})$$

The iterated Crank-Nicholson scheme is second order accurate in space and time.

-
- [1] T. Zwerger and E. Müller, *Astro. & Astrophys.*, **320**, 209 (1997).
- [2] M. Ruffert and H.-T. Janka, *Astro. & Astrophys.*, **344**, 573 (1999).
- [3] Y.T. Liu and L. Lindblom, *Mon. Not. Astro. Soc.*, **324**, 1063 (2001).
- [4] Y.T. Liu, *Phys. Rev. D*, **65**, 124003 (2002).
- [5] F.A. Rasio, and S.L. Shapiro, *Astrophys. J.*, **401**, 226 (1992); F.A. Rasio, and S.L. Shapiro, *Astrophys. J.*, **432**, 242 (1994); F.A. Rasio, and S.L. Shapiro, *Class. Quant. Grav.*, **16**, R1 (1999).
- [6] M. Shibata and K. Uryu, *Phys. Rev. D*, **61**, 064001 (2000).
- [7] In Newtonian limit, both gravitational-wave driven (CFS) and viscosity driven bar-instabilities occur for $\beta \gtrsim 0.14$ [8–10]. Relativistic effects enhance the CFS-instability [11], but suppress the viscosity-driven instability [12–14].
- [8] S. Chandrasekhar, *Ellipsoidal Figures of Equilibrium* (New Haven: Yale Univ. Press, 1969).
- [9] D. Lai, and S.L. Shapiro, *Astrophys. J.*, **442**, 259 (1995).
- [10] D. Skinner, and L. Lindblom, *Astrophys. J.*, **461**, 920 (1996).
- [11] N. Stergioulas, and J.L. Friedman, *Astrophys. J.*, **492**, 301 (1998).
- [12] S.L. Shapiro, and S. Zane, *Astrophys. J. Supp.*, **117**, 531 (1998).
- [13] T.D. Girolamo, and M. Vietri, *Astrophys. J.*, **581**, 519 (2002)
- [14] D. Gondek-Rosinska, and E. Gourgoulhon, *Phys. Rev. D*, **66**, 044021 (2002).
- [15] J. Hjorth *et al.*, *Nature*, **423**, 847 (2003).
- [16] T.W. Baumgarte, S.L. Shapiro, and M. Shibata, *Astrophys. J.*, **528**, L29 (2000).
- [17] N.D. Lyford, T.W. Baumgarte, and S.L. Shapiro, *Astrophys. J.*, **583**, 410 (2003).
- [18] M. Rampp, E. Müller, M. Ruffert, *Astro. & Astrophys.*, **332**, 969 (1998).
- [19] M. Shibata, S. Karino, and Y. Eriguchi, *Mon. Not. Astro. Soc.*, **334**, L27 (2002).
- [20] M. Shibata, S. Karino, and Y. Eriguchi, *Mon. Not. Astro. Soc.*, **343**, 619 (2003).
- [21] S. Karino and Y. Eriguchi, *Astrophys. J.*, **592**, 1119 (2003).
- [22] R. Narayan, B. Paczynski, and T. Piran, *Astrophys. J.*, **395**, L83 (1992).
- [23] A. MacFadyen, and S.E. Woosley, *Astrophys. J.*, **524**, 262 (1999).
- [24] N. Vlahakis, and A. Königl, *Astrophys. J.*, **563**, L129 (2001).
- [25] P. Mészáros, and M.J. Rees, *Astrophys. J.*, **482**, L29 (1997).
- [26] A.K. Sari, T. Piran, and J.P. Halpern, *Astrophys. J.*, **519**, L17 (1999).
- [27] T. Piran, in *Proc. of 16th Conf. on General Relativity* (Singapore: World Scientific), in press.
- [28] M.J. Rees, *Ann. Rev. Astro. & Astrophys.*, **22**, 471 (1984).
- [29] T.W. Baumgarte, and S.L. Shapiro, *Astrophys. J.*, **526**, 941 (1999).
- [30] S.L. Shapiro, to appear in *Carnegie Observatories Astrophysics Series, Vol. 1: Coevolution of Black Holes and Galaxies*, ed. L.C. Ho (Cambridge: Cambridge Univ. Press), (astro-ph/0304202).
- [31] J.M. Centrella, K.C.B. New, L.L. Lowe, and J.D. Brown, *Astrophys. J.*, **550**, L193 (2001).
- [32] M. Saijo, T.W. Baumgarte, and S.L. Shapiro, *Astrophys. J.*, **595**, 352 (2003).
- [33] M. Saijo, T.W. Baumgarte, S.L. Shapiro, and M. Shibata, *Astrophys. J.*, **569**, 349 (2002).
- [34] M. Shibata, and S.L. Shapiro, *Astrophys. J.*, **572**, L39 (2002).
- [35] K.C.B. New, and S.L. Shapiro, *Classical Quantum Gravity*, **18**, 3965 (2001).
- [36] K.C.B. New, and S.L. Shapiro, *Astrophys. J.*, **548**, 439 (2001).
- [37] Y.B. Zeldovich, and I.D. Novikov, *Relativistic Astrophysics, Vol. 1: Stars and Relativity* (Chicago: Univ. Chicago Press, 1971).
- [38] S.L. Shapiro, *Astrophys. J.*, **544**, 397 (2000), Paper I.
- [39] N. Andersson, *Astrophys. J.*, **502**, 708 (1998).
- [40] J.L. Friedman, and S.M. Morsink, *Astrophys. J.*, **502**, 714 (1998).
- [41] N. Andersson, K.D. Kokkotas, and N. Stergioulas, *Astrophys. J.*, **516**, 307 (1999).
- [42] L. Lindblom, B.J. Owen, and S.M. Morsink, *Phys. Rev. Lett.*, **80**, 4843 (1998).
- [43] L. Rezzolla, F.K. Lamb, and S.L. Shapiro, *Astrophys. J.*, **531**, L139 (2000).
- [44] L. Rezzolla, F.K. Lamb, D. Markovic, and S.L. Shapiro, *Phys. Rev. D*, **64**, 104013 (2001)
- [45] L. Rezzolla, F.K. Lamb, D. Markovic, and S.L. Shapiro, *Phys. Rev. D*, **64**, 104014 (2001).
- [46] P. Arras, E.E. Flanagan, S.M. Morsink, A.K. Schenk, S.A. Teukolsky, and I. Wasserman, *Astrophys. J.*, **591**, 1129 (2003).
- [47] A.K. Schenk, P. Arras, E.E. Flanagan, S.A. Teukolsky, and I. Wasserman, *Phys. Rev. D*, **65**, 024001 (2002).
- [48] P. Gressman, L.M. Lin, W.M. Suen, N. Stergioulas, and J.L. Friedman, *Phys. Rev. D*, **66**, 041303 (2002).
- [49] P.B. Jones, *Phys. Rev. Lett.*, **86**, 1384 (2001).
- [50] P.B. Jones, *Phys. Rev. D*, **64**, 084003 (2001).
- [51] L. Lindblom, and B.J. Owen, *Phys. Rev. D*, **65**, 063006 (2002).
- [52] J.N. Cook, S.L. Shapiro, and B.C. Stephens, *Astrophys. J.*, in press (2003) (astro-ph/0310304), Paper II.
- [53] S.A. Balbus and J.F. Hawley, *Rev. Mod. Phys.*, **70**, 1 (1998).
- [54] T.W. Baumgarte and S.L. Shapiro, *Astrophys. J.*, **585**, 921 (2003).
- [55] L.D. Landau and E.M. Lifshitz, *Fluid Mechanics* (Butterworth-Heinemann, 1987)
- [56] L.D. Landau, E.M. Lifshitz, and L.P. Pitaevskii, *Electrodynamics of Continuous Media*, (Oxford: Pergamon), p. 227.
- [57] S.A. Teukolsky, *Phys. Rev. D*, **61**, 087501 (2000).
- [58] J.-L. Tassoul, *Theory of Rotating Stars*, Princeton Univ. Press (1978).
- [59] H.-Th. Janka and R. Mönchmeyer, *Astro. & Astrophys.*, **226**, 69 (1989).
- [60] C.W. Misner, K.S. Thorne and J.A. Wheeler, *Gravitation* (Freeman, New York, 1973)

- [61] J.D. Jackson, Classical Electrodynamics, 2nd Edition (John Wiley & Sons, Inc, New York, 1975).
- [62] H. Komatsu, Y. Eriguchi and I. Hachisu, Mon. Not. R. Astro. Soc., **237**, 355 (1989); H. Komatsu, Y. Eriguchi and I. Hachisu, Mon. Not. R. Astro. Soc., **239**, 153 (1989).
- [63] Y. Eriguchi and E. Müller, Astro. & Astrophys., **146**, 260 (1985).
- [64] C. Cutler, and L. Lindblom, Astrophys. J., **314**, 234 (1987).
- [65] J.A. Pons, S. Reddy, M. Prakash, J.M. Lattimer, and J.A. Miralles, Astrophys. J., **513**, 780 (1999).
- [66] R.C. Duncan, C. Thompson, Astrophys. J., **392**, L9 (1992).
- [67] H.C. Spruit, Astro. & Astrophys., **349**, 189 (1999).
- [68] J. Heyvaerts and E.R. Priest, Astro. & Astrophys., **117**, 220 (1983).
- [69] J.W. York, in Sources of Gravitational Radiation, ed. by L. Smarr (Cambridge University Press, 1979).
- [70] According to Eqs. (142) and (172), $\Omega_c = 2\Omega_{\text{central}}$. Also, the specific angular momentum increases with $\hat{\omega}$ for this rotation law. Hence it satisfies the Rayleigh criterion of dynamical stability against axisymmetric perturbations.
- [71] According to Eqs. (142) and (189), $\Omega_c = \Omega_{\text{central}}$. This rotation law also satisfies the Rayleigh criterion for dynamical stability since the specific angular momentum increases with $\hat{\omega}$.